



HAL
open science

Brain Image Analysis, Arterial Spin Labeling Perfusion Images and Joint EEG-fMRI Neurofeedback

Pierre Maurel

► **To cite this version:**

Pierre Maurel. Brain Image Analysis, Arterial Spin Labeling Perfusion Images and Joint EEG-fMRI Neurofeedback. Computer science. Université de Rennes 1, 2021. tel-03273931

HAL Id: tel-03273931

<https://inserm.hal.science/tel-03273931>

Submitted on 29 Jun 2021

HAL is a multi-disciplinary open access archive for the deposit and dissemination of scientific research documents, whether they are published or not. The documents may come from teaching and research institutions in France or abroad, or from public or private research centers.

L'archive ouverte pluridisciplinaire **HAL**, est destinée au dépôt et à la diffusion de documents scientifiques de niveau recherche, publiés ou non, émanant des établissements d'enseignement et de recherche français ou étrangers, des laboratoires publics ou privés.



Mémoire pour l'obtention de
L'HABILITATION À DIRIGER LES RECHERCHES
de l'Université de Rennes 1

Présenté par
Pierre MAUREL

Brain Image Analysis, Arterial Spin Labeling Perfusion Images and Joint EEG-fMRI Neurofeedback

Présentée le 28 juin 2021

Devant un jury composé de :

<i>Rapporteurs :</i>	Michel Dojat	- Directeur de recherche, INSERM, France
	Florence Forbes	- Directrice de recherche, Inria, France
	Xavier Golay	- Professor, University College London, United Kingdom
<i>Examineurs :</i>	Sophie Achard	- Directrice de recherche, CNRS, France
	Patrick Bouthemy (président)	- Directeur de recherche, Inria, France

Foreword

In the ten last years, my research activities have addressed a variety of topics, however all related to the development of new methods for brain images processing and analysis, for imaging biomarkers detection and computer-aided diagnosis. In this document, I will focus on two important sub-parts of these researches: the development of new methods for processing and analyzing arterial spin labeling images, and the introduction of novel neurovascular coupling methods (electroencephalography and functional magnetic resonance imaging modalities), using *a priori* sparsity constraints, in order to improve the neurofeedback proposed for the rehabilitation of stroke patients.



Name cloud created with <https://www.wordclouds.com/> from the list of co-authors (post PhD)

Acknowledgments

I would like to thank the committee members for accepting to evaluate these researches, as well as the whole Empenn team that I have the pleasure to work with on a daily basis. Of course, my thanks go in particular to the students and post-docs with whom I had the pleasure to collaborate, and who are generally the first authors of the works presented, they are credited at the beginning of each corresponding part. And finally, a special thought for Christian, who welcomed me in Rennes in 2009, accompanied me in my discovery of the neuroimaging field, and whose absence is still keenly felt.

Contents

1	Arterial Spin Labeling	5
1.1	Robust Estimation of Cerebral Blood Flow	8
1.2	Patch-Based Super-Resolution	10
1.3	Heteroscedasticity and Detection of Perfusion Abnormalities	12
1.4	<i>A contrario</i> Detection of Perfusion Abnormalities	14
1.5	Impact of Acquisition Time in Resting-State ASL	16
2	Joint EEG-fMRI neurofeedback	19
2.1	Electrodes Detection During Simultaneous EEG/fMRI	22
2.2	Multimodal EEG and fMRI Source Estimation	24
2.3	Prediction of Multimodal Neurofeedback Scores from EEG	26
3	Conclusions and Perspectives	29
3.1	Arterial Spin Labeling Images Processing and Analysis	30
3.1.1	Multiparametric estimation	30
3.1.2	Functional connectivity estimation	30
3.1.3	Pediatric applications	31
3.2	Portable and Personalized Neuro-Rehabilitation with Multimodal Neurofeedback	33
3.2.1	Personalized neurofeedback based on brain connectivity and graph signal processing	33
3.2.2	Towards a more portable neurofeedback	34
	List of Acronyms	36

1

Cerebral Perfusion, Arterial Spin Labeling, Image Processing and Analysis

Cerebral perfusion is the delivery of oxygen and nutrients from the blood to the brain tissue. It is mainly studied at the level of microcirculation, which takes place in the finest vessels of the blood system, the capillaries. Several medical imaging modalities can be used to evaluate this perfusion, such as nuclear imaging, computed tomography and magnetic resonance imaging. Table 1, from [113], summarizes the main characteristics of each of the main modalities available. The foremost advantages of Arterial Spin Labeling (ASL) over other modalities are therefore: its non-invasiveness, facilitating the study of brain perfusion in healthy subjects, and its ability to quantify perfusion parameters, allowing patient-specific studies. As a matter of fact, different parameters are encountered in the literature to characterize this perfusion and, under some assumptions, ASL is able to quantify some of them. The most commonly parameters mentioned in ASL are Cerebral Blood Flow (CBF), usually expressed in milliliters of blood per minute per 100 grams of brain tissue, and Arterial Transit Time (ATT), expressed in seconds or milliseconds. Investigating cerebral perfusion in general and these parameters specifically, is of interest in many pathologies [52], such as cerebral vascular disorders, cancers, dementias, certain psychiatric diseases or epilepsy. Perfusion is also a relatively direct indicator of cerebral activity, allowing to obtain functional magnetic resonance images.

Introduced in the early 1990's [37], ASL is a Magnetic Resonance Imaging (MRI) perfusion technique based on the use of an endogenous tracer: the protons of blood water. As illustrated in figure 1, the principles of this modality is to acquire two images: a first one (Label) with prior labeling of the incoming blood and a second one (Control) without. The image obtained after subtraction between the Control and the

Table 1: Reproduced from [113]: Overview of the Imaging Techniques Dedicated to Brain Hemodynamics, with a focus on Arterial Spin Labeling and its main features

	Brain Perfusion Imaging Techniques						
	PET	SPECT	XeCT	PCT	DSC	ASL	Doppler
Feasibility							
Age range	Adults (and children for static exams)	Adults (and children)	Adults (and children)	Adults (and children)	Adults (and children)	Adults + children	Adults + children
Bedside	No	In some instances	No	No	No	No	Yes
Contrast material	$^{15}\text{O}_2$, C^{15}O_2 , H_2^{15}O	^{133}Xe , $^{99\text{m}}\text{Tc-HMPAO}$, $^{99\text{m}}\text{Tc-ECD}$, $^{123}\text{I-IMP}$ (diffusible)	Stable xenon gas (diffusible)	Iodinated contrast material (nondiffusible)	gadolinium chelate (nondiffusible)	None (endogenous contrast)	None (endogenous contrast)
Radiation/study	0.5–2 mSv	3.5–12 mSv	3.5–10 mSv	2–3 mSv	None	None	None
Data acquisition	5–9 min	10–15 min	10 min	40 sec	1 min	5–10 min	10–20 min
Data processing	5–10 min	5 min	10 min	5 min	5 min	5 min	None
Assessed parameters	CBV, CBF, rOEF, glucose metabolism	CBF	CBF	CBF, CBV, MTT, TTP, permeability map	CBF, CBV, MTT, TTP, permeability map	CBF	ICA BFV
Quantitative accuracy	Yes	Yes for ^{133}Xe and $^{123}\text{I-IMP}$; no for the others tracers	Yes	Yes	Not in daily practice	Yes	Yes for hemispheric CBF
Including for low perfused areas†	Yes	Not applicable	Yes	Yes	Not applicable	Not <10 mL/min/100 g	Not applicable
Reproducibility	5%	10%	12%	10–15%	10–15%	10%	5%
Brain coverage	Whole brain	Whole brain	6-cm thickness	4–5 cm thickness	Whole brain	Whole brain	One measurement for each hemisphere
Spatial resolution	4–6 mm	4–6 mm	4 mm	1–2 mm	2 mm	2 mm	Not applicable
Minimal time interval between 2 successive exams	10 min	10 min (split-dose technique for $^{99\text{m}}\text{Tc-HMPAO}$, $^{99\text{m}}\text{Tc-ECD}$ and $^{123}\text{I-IMP}$)	20 min	10 min	25 min	0 min	0 min

†“Quantitative accuracy in low perfusion areas” is meant to report which imaging techniques are quantitatively accurate even in case of altered hemodynamics areas, for example, in ischemic areas.

Label images is perfusion-weighted: the signal of a voxel is stronger the more the labeled blood arrived at this location. Figure 2 describes the evolution, in a given voxel, of the difference signal between the Label and Control images. In [23], Buxton and colleagues proposed a simple model of this temporal evolution, depending on some parameters: CBF, ATT, labeling efficiency, equilibrium magnetization of arterial blood, and relaxation time of blood and tissues. Interestingly, to a first approximation, the model no longer depends on the arrival time in its decreasing part, enabling the quantification of CBF, if the Inversion Time (TI) is chosen in this second part.

However, ASL has some drawbacks, the main one being its low signal-to-noise ratio, which explains why its use was initially limited mainly to research protocols. This also justifies the need for processing and analysis tools specifically dedicated to this imaging modality. The development of such tools, as well as the improvement of the acquisition sequences, and the considerable standardization efforts of the community [4, 48] have resulted in recent years in an important maturation of ASL’s position in the clinic.

In the following sections, I will present some of our contributions over the past ten years: robust estimation of cerebral blood flow, patch-based super-resolution, heteroscedasticity and detection of perfusion abnormalities, *a contrario* detection of perfusion abnormalities, and impact of acquisition duration in resting-state ASL. Each of them will be synthesized on a double page and the interested reader can refer to the publications listed at the end of the pages for more details. The figures presented are generally extracted from the above mentioned publications. These contributions are the result of three theses that I co-supervised: those of Camille Maumet, Cédric Meurée and Corentin Vallée.

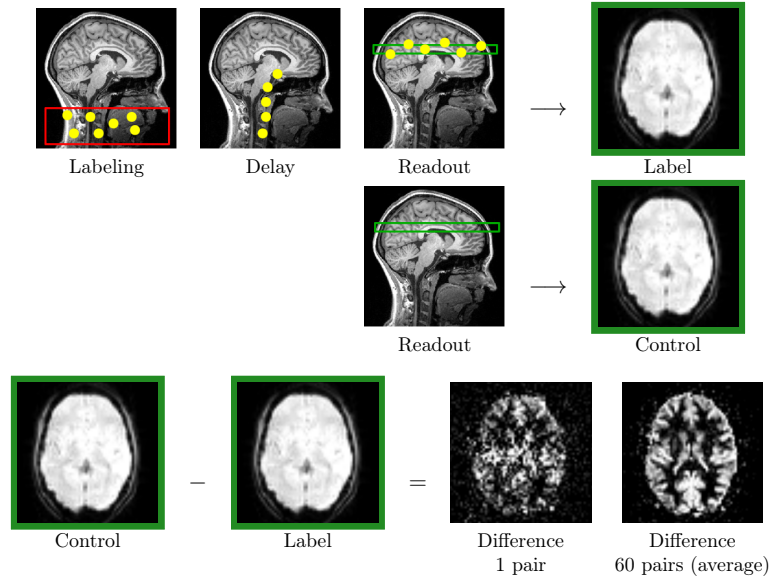


Figure 1: Principles of a typical ASL acquisition: two images are acquired, a first one (Label) with prior labeling of the incoming blood and a second one (Control) without. The image obtained after subtraction between the Control and the Label images is perfusion-weighted: the signal of a voxel is stronger the more the labeled blood arrived at this location.

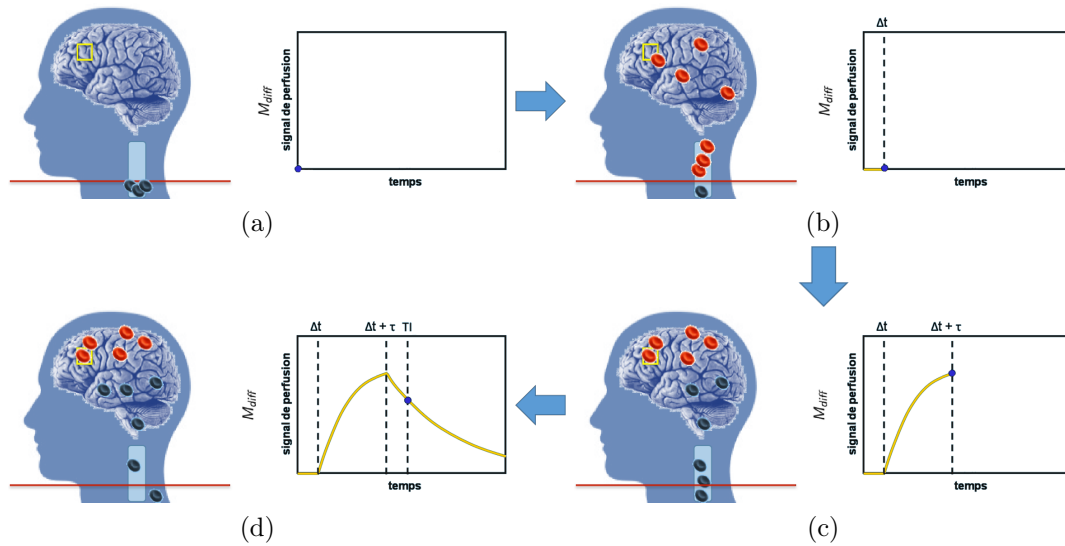


Figure 2: Evolution of the difference signal in a voxel (yellow square) between the Label and Control images, from the labeling to the acquisition. (a) Labeling has just been performed (red line): the labeled blood has not yet arrived in the voxel of interest. (b) After Δt , the arterial transit time, the labeled blood starts to arrive. (c) After $\Delta t + \tau$, the labeling duration, all the labeled blood is arrived. (d) After TI, inversion time, the signal is decreasing due to relaxation and venous clearance, and the Label image is acquired.

Robust Estimation of Cerebral Blood Flow



Context Due to the low Signal-to-Noise Ratio (SNR) of the ASL sequence, a single pair of control and label images is not sufficient to measure perfusion. The acquisition is therefore repeated several times, leading to n pairs of images (usually $n \geq 30$).

Perfusion information is then usually extracted by pair-wise subtracting the control and label images (or using surround subtraction) and averaging across the repetitions.

Though sample mean, as an unbiased estimate of mean, ensures convergence as n grows, it has a breakdown point of 0% (i.e. a single arbitrary large value can induce an arbitrary large estimate) and is thus very sensitive to outliers as illustrated in fig. 3.

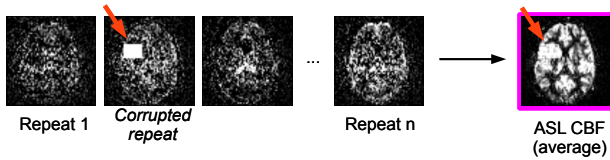


Figure 3: Sensitivity of the sample mean to outliers.

And yet it is well-known that instabilities during the acquisition and improperly corrected patient motion can cause artefactual values. In particular, sudden subject motion often induces strong corolla-shaped artefacts [102].

To avoid the detrimental effects that a few abnormal repetitions could have in the final perfusion map, it is often suggested to ignore the volumes corresponding to the motion peaks using an appropriate threshold [102]. Volumes with (estimated) motion parameters greater than $[1 - 3]^\circ$ or $[1 - 3]$ mm are thus discarded before averaging. However the choice of these thresholds is empirical and there is no common rule across studies or automatic methods to tune these ad-hoc parameters. In [104], the authors proposed an automatic algorithm for outliers rejection in ASL perfusion series based on z-score thresholding at the volume (or slice) level. Their method produced satisfactory results on a qualitative validation based on ratings made by medical experts. However, their approach is based on z-scores, while more robust statistical measures are known to be better suited to deal

with outliers. Also, they rely on empirically tuned parameters that might limit the generalization of their procedure to new datasets.



Contribution How to appropriately deal with outliers has been widely studied in the statistical literature and a large range of methods has emerged. Z-score is known to be sensitive upon sample size and is suffering from masking effects when more than one outlier is present in the series [100]. Indeed, in a dataset containing more than one outlier, the standard deviation estimate will be artificially inflated which may prevent z-score based outlier detection. On the other hand, M-estimators are robust techniques to estimate location and scale in the presence of outliers. In [75], we investigated the use of Huber's M-estimator [54], as it is the most widely used. An example of estimate computed with this method is provided in fig. 4.

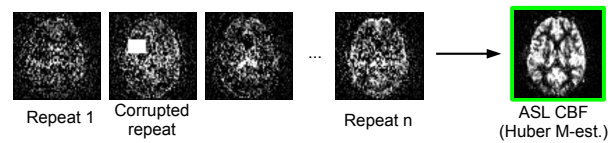


Figure 4: Robust ASL CBF map via Huber's M-estimator.

A theoretically more efficient approach to deal with outliers is indeed to employ robust statistics, such as M-estimators. In [54], M-estimators are defined, given a function ρ , as solutions $\hat{\theta}$ of:

$$\hat{\theta} = \arg \min_{\theta} \left(\sum_{i=1}^n \rho(x_i - \theta) \right). \quad (1)$$

If ρ is differentiable, and ψ is its derivative then eq. (1) can be solved by finding the root of $\sum_{i=1}^n \psi(x_i - \theta) = 0$. The sample mean can be seen as an M-estimator with $\rho(x_i - \theta) = (x_i - \theta)^2$ and $\psi(x_i - \theta) = 2(x_i - \theta)$ leading to $\hat{\theta} = \frac{1}{n} \sum_{i=1}^n x_i$.

The M-estimator of location proposed by Huber

in [54] is defined by:

$$\psi(x_i - \theta) = \gamma\left(\frac{x_i - \theta}{\sigma}\right) \quad \text{where}$$

$$\gamma(x) = \begin{cases} -k, & x < -k, \\ x, & -k < x < k, \\ k, & x > k. \end{cases}$$

Classical values for k and σ are respectively 1.345 (corresponding to 95% efficiency in Gaussian data) and the median absolute deviation divided by 0.6745. Huber's M-estimator is applied voxel by voxel on the perfusion-weighted series to obtain the robust perfusion-weighted map. Fig. 5 illustrates the $\psi(x)$ functions for the three estimators of interest.

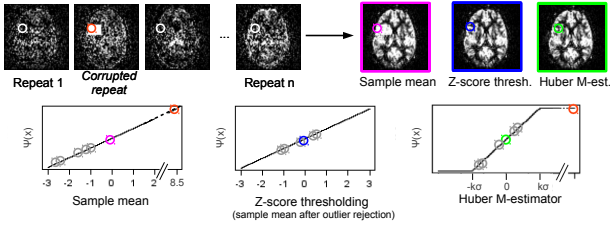


Figure 5: ψ functions for three estimators: sample mean, z-score thresholding (equivalent to a sample mean after outlier rejection), Huber's M estimator.

Validation and Results

The impact of using the M-estimator on the CBF quantification was evaluated in two different ways: on simulated data and on subjects diagnosed with brain tumor.

- On simulated data: a given percentage of ASL volumes was corrupted by adding samples drawn from a uniform distribution to a given percentage of the voxels (three levels of corruption: 2%, 20% or 50%) per volume. As seen in fig. 6, in the presence of outliers, Huber's M-estimator is always more accurate than the sample mean and either better or as good as z-thresholding.
- On clinical data: for these 24 cancer patients, Dynamic Susceptibility weighted Contrast (DSC) imaging had also been acquired. The quality of the maps produced by each method was therefore measure through the Pearson linear correlation coefficient with the DSC CBF map. As shown in fig. 7, the M-estimator still provides the best estimation, even though the difference with the other methods are less important.

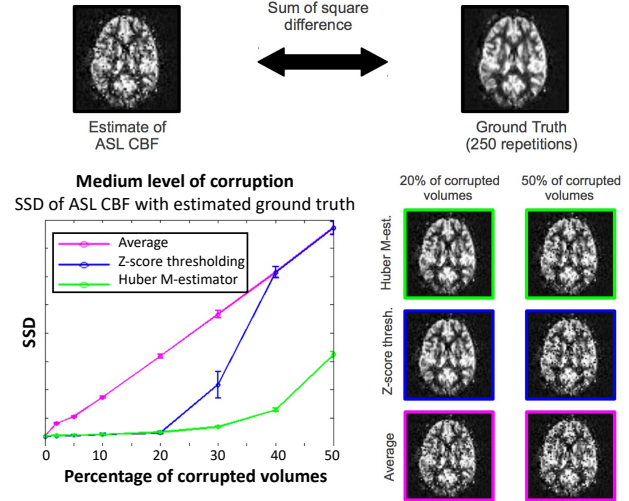


Figure 6: Healthy subject with simulated outliers: sum of squared differences (SSD) of ASL CBF map, computed by M-estimator, z-score thresholding and sample mean, with the estimated ground truth.

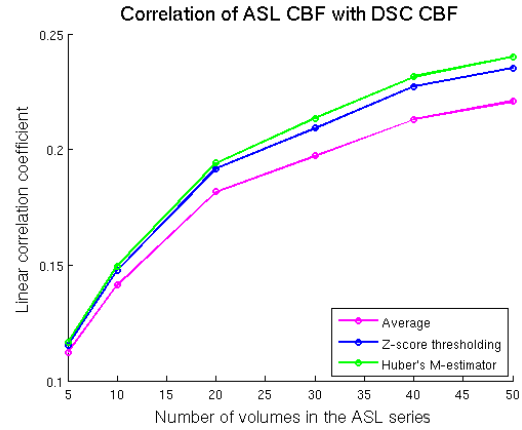


Figure 7: Clinical dataset: correlation of ASL CBF with DSC CBF for different number of repetitions.

Take-Home Message

- Outlier filtering provides more robust CBF maps than the sample mean
- As M-estimators are able to deal with a broader range of outliers, we recommend the use of M-estimators as robust method to compute ASL CBF maps

Main Related Publications: [74, 75, 71]

Patch-Based Super-Resolution



Context

Fast acquisition techniques such as echo planar imaging are required to image the dynamic process of the labeled protons circulation, generating low resolution and SNR images. As seen previously, averaging a number of repetitions is thus necessary, making ASL sensitive to new potential corruptions, such as motion artifacts. Moreover, voxel-wise estimations of perfusion parameters are perturbed by the low image resolution. Indeed, this leads to the introduction of partial volume effects, meaning that perfusion of different tissues contributes to the perfusion signal observed in a single image voxel. In clinical conditions, acquiring ASL at higher resolution is a challenging task, usually implying either a decrease in SNR, or an increase in acquisition time.

Other MR modalities are facing similar low resolution properties, such as T2-weighted and diffusion images. Classical interpolation methods can be applied to MR images, but introduce a smoothing effect. To overcome this, Super Resolution (SR) approaches aim to reconstruct high frequency information from low resolution data. Some of these methods are based on multiple low resolution acquisitions, therefore requiring specific acquisition protocols, which can be time consuming [98]. On the other hand, several authors [96, 27] have adapted and extended non-local patch-based SR approaches that are independent of the acquisition process to the MRI domain. The main idea consists in using self similarities in images to perform reconstructions at higher resolution.



Contribution

In [80], we proposed a novel method to increase the resolution of ASL images, taking advantage of a High Resolution (HR) GMstructural image, typically acquired in conventional imaging protocols. This non-local patch-based approach for ASL reconstruction relies on the assumption of similar spatial patterns between the perfusion image and the high-resolution structural image. This hypothesis of shared anatomical properties between structural and ASL images seems natural, since gray and white matter are the two tissues that contribute to the brain ASL signal, with their own perfusion

characteristics (e.g. CBF and arterial transit time). This new method increases the resolution of ASL images without lengthening the acquisition time.

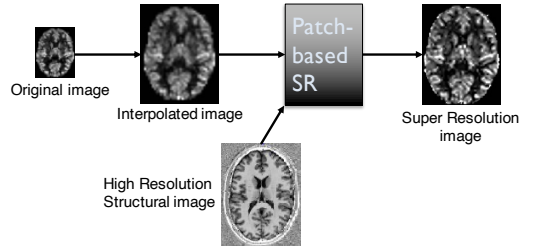


Figure 8: Principle of the proposed method.

As illustrated in fig. 8, the proposed method starts by a third order B-splines interpolation applied to the low resolution image in order to increase its dimension to the desired one. This initialization is followed by iterations between a non-local patch-based regularization and a fidelity term assuring the global intensities mean consistency between the initial low resolution image and the reconstructed one.

The regularization step, similar to the non-local means denoising method [21], corresponds to a patch averaging using a similarity term between voxels' neighborhoods. In our case, this patch similarity is assessed both through the perfusion image and the structural one

$$X_i^{t+1} = \frac{1}{Z_i} \sum_{j \in V_i} X_j^t e^{-\text{Sim}(X^t, i, j) - \lambda \text{Sim}(X_s, i, j)}$$

X_i^t is the intensity of voxel i in the image X^t corresponding to the reconstructed perfusion image at iteration t . X_s is the structural image. V_i is the correspondence search volume around voxel i and Z_i a scaling parameter controlling that the sum of the exponential weights is equal to 1. $\text{Sim}(A, i, j)$ is a term measuring the similarity between the neighborhoods of voxel i and j in the image A , defined as follows

$$\text{Sim}(A, i, j) = \frac{1}{\sigma_i^2} \|N(A_i) - N(A_j)\|_{\mathcal{L}_2}^2$$

where $N(A_i)$ is a patch around voxel i in the image A and σ_i^2 the empirical local variance. It is important to note that only values present in the perfusion image

are averaged, the structural image is only involved in the definition of the weights in this average.

The global low resolution mean value consistency corresponds to an additive offset equal to the difference between the mean image value of X^t and the mean of the initial low resolution image Y , respectively $\mu(X^t)$ and $\mu(Y)$: $X^{t'} = X^t + \mu(Y) - \mu(X^t)$.

Iterations between these two steps are performed until convergence.

Validation and Results

The quality of the produced super-resolution perfusion images was evaluated in three different ways:

- On simulated data: a structural image was acquired and segmented using SPM12 algorithm, providing probability maps for gray matter (GM) and white matter (WM), noted p_{GM} and p_{WM} . An artificial CBF map was produced using fixed CBF values for GM and WM: $CBF_i = 70 * p_{GM,i} + 25 * p_{WM,i}$. This simulated high-resolution perfusion images was then down-sampled and corrupted by some noise, and our SR method was applied and compared to classic interpolation. As shown in fig. 9, our reconstruction is always closer to the original HR image.

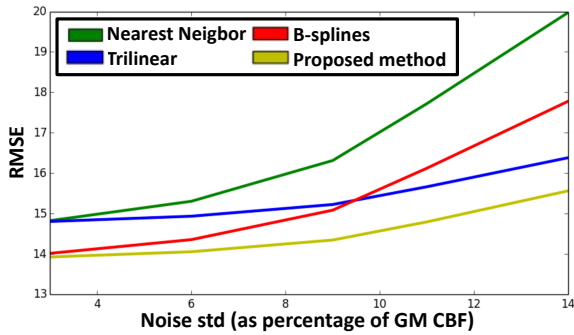


Figure 9: Root mean square errors between the HR simulated CBF image and the reconstructed images.

- On healthy subjects: for 4 subjects, we acquired standard pseudo-Continuous ASL (pCASL) images with resolution $3.5 \times 3.5 \times 3.5 \text{ mm}^3$ and 30 repetitions, a high-resolution structural image, and another series of pCASL images, with resolution of $1.75 \times 1.75 \times 2.5 \text{ mm}^3$ and 100 repetitions. Two corresponding CBF maps were thus estimated, one considered as low-resolution and the other as ground truth. Again, our super-resolution method provides images closest (ac-

ording to RMSE values) to the HR acquired ones. Fig. 10 shows an example of such images.

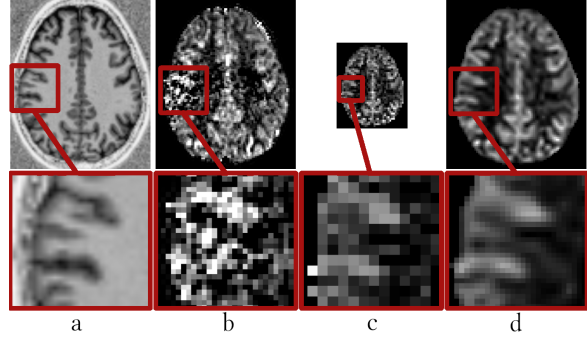


Figure 10: Healthy subject: a) structural image, b) CBF maps from the acquired HR pCASL., c) low resolution pCASL acquisitions, d) proposed SR reconstructed CBF.

- On clinical data: on the same data as in the previous section, from the acquired $3 \times 3 \times 7 \text{ mm}^3$ PASL sequence, we estimated HR CBF maps using our super-resolution method and compared it to the DSC CBF with a resolution of $1.8 \times 1.8 \times 4 \text{ mm}^3$. As shown in fig. 11, our method also improves the correlation to the DSC CBF map.

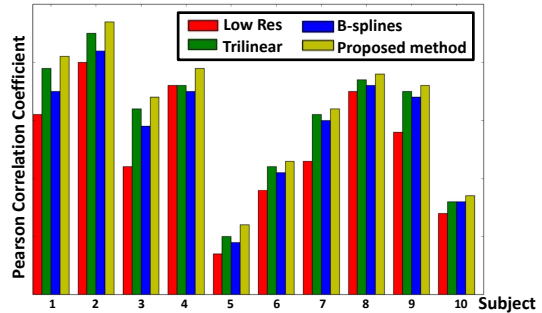


Figure 11: Pearson correlation between the reference DSC CBF maps and the different reconstructed images.

Take-Home Message

- Patch-Based super-resolution outperforms interpolation techniques
- Independent of segmentation methods
- No need for extended acquisition time

Main Related Publications¹: [79, 80, 78]

¹The SR method was included in the Siemens *MR ASL Perfusion Analysis prototype*, as a syngo.via Frontier application.

Heteroscedasticity and Detection of Perfusion Abnormalities



Context

Patient-specific abnormal perfusion patterns are useful biomarkers for the diagnosis and monitoring of patients with a range of pathologies involving microvascular dysfunction. The quantification of CBF from ASL images can be used for estimating patient-specific perfusion abnormalities, by comparing a single patient to a group of healthy controls. The most widespread approach to compare voxel-wise maps in neuroimaging is the massively univariate General Linear Model (GLM). To detect differences between two groups with repeated measurements, a subtype of GLM is generally used: a mixed-effect hierarchical two-sample t-test with two levels, subject and group. In this context, two variance components are of interest: the within-subject variance (or the measurement error, estimated from the repeated ASL acquisitions of a single subject) and the between-subject variance.

In the functional MRI community, where similar statistical models are applied, two approaches are currently in use to solve hierarchical GLMs [82, 25]. On the one hand, the homoscedastic approach assumes homogeneous within-subject variances or negligible within-subject variances by comparison to between-subject variance. On the other hand, the heteroscedastic approach models heterogeneous within-subject variances. The latter is theoretically more efficient in the presence of heterogeneous variances but algorithmically more demanding. The practical superiority of the heteroscedastic approach for fMRI studies is still under debate and both approaches are in use in the community: SPM favors the homoscedastic approach, while FSL and AFNI use the heteroscedastic model.

Due to the low SNR of ASL sequences, within-subject variances have a significant impact on the estimated perfusion maps and the heteroscedastic model might be better suited in this context.



Contribution

In [77], we investigated the performance of the homoscedastic and heteroscedastic approaches, in terms of specificity and sensitivity in detecting patient-specific perfusion abnormalities

from ASL images.

In ASL, at the subject level, the data under study is a 4D volume of CBF maps containing r volumes. The observations are therefore repeated measurements of the same underlying value. For a subject and at a given voxel, this perfusion value can be estimated by averaging the values for each repetition: $\hat{\beta}_s = \frac{1}{r} \sum_{i=1}^r y_{s,i}$, where $y_{s,i}$ correspond to the value for subject s and repetition i . Similarly, the sampling variance of $\hat{\beta}_s$ is estimated by:

$$\widehat{\text{Var}}(\hat{\beta}_s) = \frac{\hat{\sigma}_s^2}{r} \quad \text{where} \quad \hat{\sigma}_s^2 = \frac{1}{r-1} \sum_{i=1}^r (y_{s,i} - \hat{\beta}_s)^2.$$

Given a group of n subjects, we assume that subjects 1 to $n-1$ are part of the control group and subject n is the patient of interest. Then, the one-versus-many second-level model is defined by

$$\begin{bmatrix} \hat{\beta}_1 \\ \vdots \\ \hat{\beta}_{n-1} \\ \hat{\beta}_n \end{bmatrix} = \begin{bmatrix} 1 & 0 \\ \vdots & \vdots \\ 1 & 0 \\ 0 & 1 \end{bmatrix} \begin{bmatrix} \beta_{controls} \\ \beta_{patient} \end{bmatrix} + \gamma_{G_C}. \quad (2)$$

$\beta_{controls}$ and $\beta_{patient}$ are the two perfusion parameters to be estimated and compared. The error term γ_{G_C} contains two combined sources of variations: the within-subject variance and the between-subject variance. Each element of γ_{G_C} is therefore assumed to follow a normal distribution: $\gamma_{G_C}^s \sim \mathcal{N}\left(0, \sigma_G^2 + \frac{\sigma_s^2}{r}\right)$.

Solving eq. (2) gives an estimate of the patient versus control group contrast, $\hat{b} = \hat{\beta}_{controls} - \hat{\beta}_{patient}$, and its associated sampling variance, $\widehat{\text{Var}}(\hat{b})$. In the general heteroscedastic model as stated above, the system (2) is solved by using a weighted least square. Under the homoscedastic assumption, assuming homogeneous within-subject variances or negligible within-subject variances by comparison to between-subject variance, one can state that $\gamma_{G_C}^s \sim \mathcal{N}(0, \sigma_{G_C}^2)$ where $\sigma_{G_C}^2$ is the combined within- and between-subject variance. In that case, eq. (2) can be solved using Ordinary Least Squares. A detailed calculation of the homoscedastic and heteroscedastic estimates can be found, for example, in [82] or [12].

Validation and Results

21 patients diagnosed with brain tumors and 35 healthy volunteers were involved in this study. Pulsed ASL (PASL) images were acquired using a PICORE Q2TIPS sequence, and CBF maps were estimated using the kinetic model [23]. On the control group, three standard deviation estimates were then computed and are displayed in fig. 12, as well as the mean perfusion estimate, giving a template of normal perfusion.

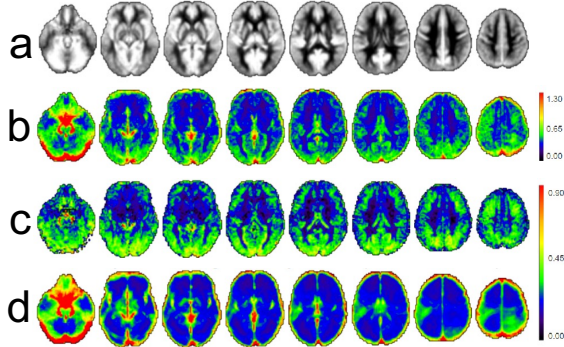


Figure 12: Control group. a) Mean perfusion estimate $\hat{\beta}_{controls}$. b) Combined within- and between-subject standard deviation estimate from the homoscedastic model $\hat{\sigma}_{G_C}$. c) Between-subject standard deviation estimate from the heteroscedastic model $\hat{\sigma}_G$. d) Root square of the average within-subject variance.

We then proved that none of the two possible assumptions behind the homoscedastic model is verified. Indeed, by comparing the two last rows in fig. 12, the within-subject variance is not negligible by comparison to the between-subject variance. Furthermore, by comparing within-subject standard deviation in different control subjects and in patients (not displayed here), variations across subjects of the within-subject variance were found to be important.

Finally, we detected perfusion abnormalities in each patient, by performing statistical tests, comparing the control group and the considered patient, for each model: homoscedastic and heteroscedastic. These abnormalities were then compared to a ground truth obtained, taking advantage of the complementary anatomical (T1w-Gd, T2w FLAIR) and perfusion (DSC) information, and visually inspected by an expert neuro-radiologist.

Fig. 13 shows these detections for one patient. Modeling heterogeneous variances (heteroscedastic model) reduces the false positive detections while preserving the true detections. Finally, we compared the

sensitivity and specificity of the two models for different smoothing kernels, with Receiver-Operating-Characteristics (ROC) curves, shown in fig 14.

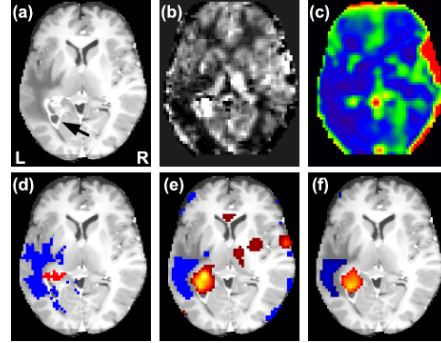


Figure 13: Detections of perfusion abnormalities in a cancer patient. a) T1w-Gd map, black arrow indicates the tumor site. b) ASL CBF estimate $\hat{\beta}_n$. c) Within-subject standard deviation $\hat{\sigma}_n^2$. d) Ground truth hypo- (blue) and hyper- (red) perfusions. Detections obtained with the homoscedastic (e) and heteroscedastic (f) models.

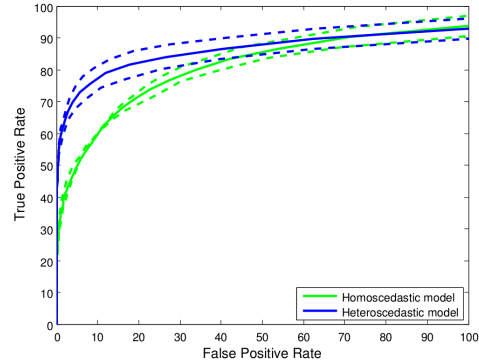


Figure 14: ROC curves for perfusion abnormality detections with the homoscedastic and heteroscedastic models. The average ROC curves across the studied smoothings are plotted in plain line. Dotted lines are plotted one standard deviation away from the average.

Take-Home Message

- The assumption of homoscedasticity is violated in ASL studies
- Modeling heteroscedasticity is essential in the detection of patient-specific perfusion abnormalities with ASL

Main Related Publications: [77, 71]

A *contrario* Detection of Perfusion Abnormalities



Context

Perfusion abnormalities are promising biomarkers for a range of pathologies. Since ASL is a quantitative imaging modalities, it is a natural candidate to obtain such detection in patient-specific studies. Inference at the patient level is highly desirable in order to perform a diagnosis or provide a personalized treatment. Furthermore, some pathologies (such as brain tumors, stroke, or some types of epilepsy) are intrinsically not well-suited to perform group voxel-wise analyses, as the pattern of spatial abnormalities is different for each patient. As described in the previous section, in [77], we showed that using a heteroscedastic GLM should be favored in ASL studies on single patients. This has, for example, been later applied in epileptic patients [17].

In neuroimaging, Gaussian smoothing is typically applied on preprocessed data before computing the GLM to compensate for small misregistrations, to reduce the effect of potential outliers and to insure that the residuals follows a Gaussian random field [90]. While smoothing has demonstrated its usefulness, its use can be problematic in some brain pathologies where the co-localization of hypo- and hyper-perfusions is common. For instance, in brain tumor, ring-enhanced lesions present a pattern of abnormal perfusion in which a central, hypo-perfused, necrosis is surrounded by an enhanced, hyper-perfused, ring.



Contribution

In [76], we presented a new locally multivariate procedure to extract patterns of abnormal perfusion in individual patients. This *a contrario* approach uses a metric from the computer vision community [36], suitable to detect abnormalities even in the presence of nearby hypo- and hyper-perfusions. This method takes into account local information without applying Gaussian smoothing to the data. As shown in fig. 15, the *a contrario* probability estimation is based on a two-step procedure.

First, a voxel-wise background model is defined. In our case, this model will come from a control population. The standard univariate GLM, but on unsmoothed data, can be used to produce the input voxel-wise probability map of the *a contrario*.

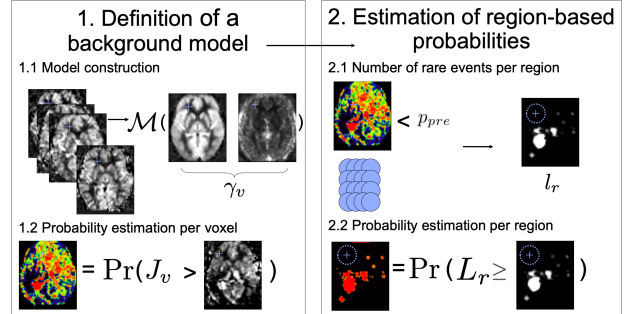


Figure 15: General principles of the *a contrario* approach.

In the second step, in order to estimate locally multivariate probabilities, we start by choosing a partition of the image into sub-regions. In our case, since the expected detections shape is unknown, the sub-regions are arbitrary defined as spheres centered at each voxel. A model to estimate the locally multivariate probability in a given region of interest from the univariate voxel-based probabilities now needs to be defined. This involves the notion of “rare events”. By definition, a rare event occurs at voxel v if the univariate probability (under the null hypothesis) to observe such value, or a more extreme, is smaller than a pre-defined threshold p_{PRE} . The initial voxel-wise probability map is thus thresholded to produce a binary map. Then, the number of rare events in a region r , $l_{(r)}$, is counted and the corresponding random variable $L_{(r)}$ follows a distribution equal to a sum of Bernoulli distributions with probability p_{PRE} :

$$L_{(r)} = \sum_{v \in r} K_{(v)} \quad \text{with} \quad K_{(v)} \sim \text{Bern}(p_{PRE})$$

The t-statistic used in massively univariate GLM, is therefore replaced by a locally multivariate statistic here: the number of rare events $l_{(r)}$ in a region r . To be able to make inference, we must now determine the distribution of the statistic $l_{(r)}$ under null hypothesis.

The original *a contrario* approach assumes spatial independence of the residuals [36] and $L_{(r)}$ then follows a binomial distribution. However, spatial autocorrelation of the residuals is a well-known phenomenon in MRI (e.g. [110] for ASL), and cannot

be disregarded. That is why, to estimate the probability of observing a given number of rare events per sphere, we proposed in [76] a non-independent probability, based on the joint distribution of a multivariate Gaussian, and introduced a corresponding estimation method. Finally, the probability associated to each region is assigned to its center voxel v to produce a voxel-wise probability map. This map can then be thresholded, taking into account a multiple comparisons correction, to obtain a detection map.

Validation and Results

To evaluate the impact of this new locally multivariate procedure, we used again the 21 patients diagnosed with brain tumors and the associated ground truth, described in the previous section. To construct the "background" model of normal perfusion, 60 controls subjects were included. Our detections were compared to standard GLM framework using seven different smoothing kernels. The detections were estimated on each patient individually, by comparing them to the control group, and individual ROC curves were calculated. For a global view of the results, the average ROC curves are shown in fig. 16, for different sets of parameters.

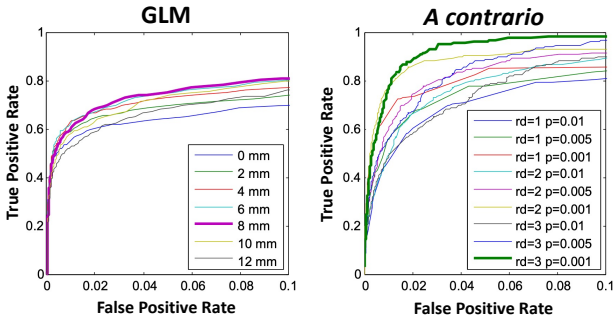


Figure 16: Average ROC curves, on 21 patients, for GLM and different smoothing kernels and for the *a contrario* approach and different sphere radii rd and p_{PRE} .

For illustration purposes, fig. 17 shows two representative patients and compares the methods at fixed false positive rate and true positive rate. The best set of parameters identified for each patient were used.

Finally, we investigated the validity of the statistical models by GLM and by the *a contrario* approach. To this aim, we checked the distribution of the p -values under the null hypothesis, by studying the control group by leave-one-out cross-validation (no hypo- or hyper-perfusion is expected). Fig. 18 plots the observed two-tailed probabilities against the ex-

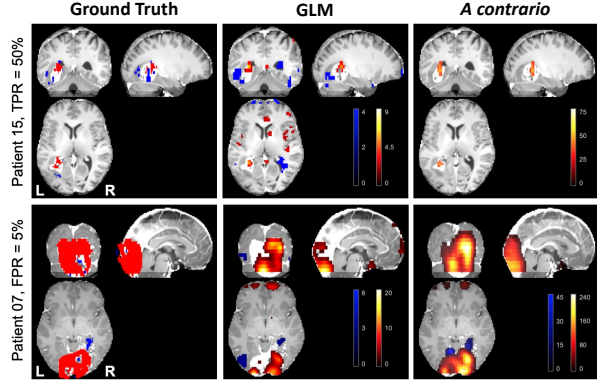


Figure 17: Perfusion abnormalities detections in two patients with the GLM and *a contrario* approach using the best parameter sets. Hyper-perfusions (red) and hypo-perfusions (blue) are overlaid on the T1w-Gd map.

pected probabilities for the standard and the non-independent *a contrario* approaches along with the GLM. The proposed non-independent *a contrario* approach provides a distribution that is closer to the theory than the standard *a contrario* and the GLM.

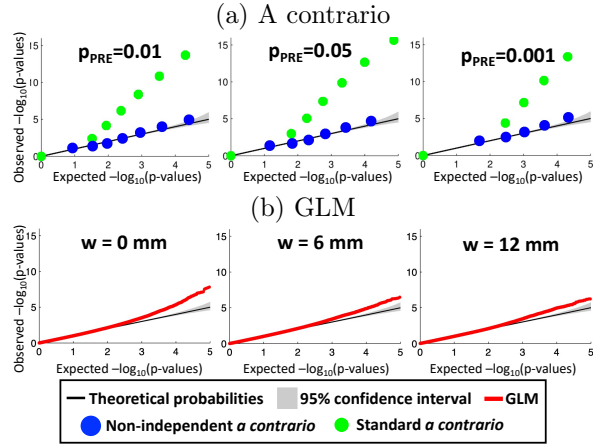


Figure 18: QQ-plots of (a) *a contrario* region-based probabilities, (b) GLM voxel-wise probabilities.

Take-Home Message

- The *a contrario* approach outperforms the standard General Linear Model.
- Non-independent probabilities provide more valid statistics in ASL analysis.

Main Related Publications: [72, 73, 76, 71]

Impact of Acquisition Time in Resting-State ASL



Context

Blood Oxygenation Level Dependent (BOLD) fMRI is now a widely used imaging technique to study cerebral activity. BOLD is however an indirect measure, and cerebral blood flow changes resulting from neuronal activity are a closer indication of brain function. Nevertheless, before the introduction of ASL, they could only be measured by invasive imaging techniques using exogenous contrast agents. Allowing quantitative and non-invasive measurement of CBF, ASL is therefore a good candidate to be an alternative to BOLD.

In Resting State fMRI (rs-fMRI), no task is given and the fluctuations of voxels time-series induced by spontaneous neuronal activations are studied [16]. The similarities in neural activation patterns define the functional connectivity of the brain, and show that the underlying cerebral architecture is organized into functional specialized units, called networks. Resting-state functional imaging aims to identify functional networks of the brain and to describe their interaction. As the resting state is not very burdensome for the subjects, especially for children and elderly people, but also for cognitive impaired patients, rs-fMRI has found clinical applications in the study of diseases and gained interest in the community in the last years.

Acquisition time is an important parameter in an rs-fMRI study with strong practical consequences. Most current rs-ASL studies use acquisitions of 8 to 13 min duration. While the influence of acquisition time in rs-BOLD has been investigated by several authors, such as [18, 15, 5], in rs-ASL it had not yet been explored.



Contribution

In [107], we focused on assessing the feasibility of ASL as an rs-fMRI method and investigating the effect of acquisition time on the estimation of individual functional networks. Seven healthy subjects were scanned using a long pCASL sequence: TR=3500ms, 420 acquired volumes, corresponding to a total acquisition time of 24 min 30 s. Each raw pCASL series was divided into 46 subseries of different lengths, from 2 min to the whole acquisi-

tion time, and the preprocessing was performed independently on each subseries.

Individual functional networks were estimated by Seed Based Analysis (SBA), whose principle is to construct areas with a homogeneous functional signal. A region of interest, called seed, is defined. Then, with a chosen similarity measure (linear correlation in our case), the voxels whose signals are synchronized to this seed are grouped together. Twenty seeds were defined from single voxels spread across six expected functional networks: Default Mode Network (DMN), Sensori-motor, Language, Salience, Visual and Cerebellum. Each seed provides a linear correlation map that was thresholded after statistical testing.

In order to assess the quality of the obtained networks, we relied on an atlas of seventeen resting-state functional networks containing our six networks of interest, the Multi-Subject Dictionary Learning atlas (MSDL) [108]. Such an atlas will naturally not provide a high quality ground truth since it does not take into account inter-individual variability for example. In our case, however, our objective is to study the relationship between acquisition time and the quality of the networks obtained, and this atlas provides a consistent measure.

Each detected network was then compared to the atlas networks, using two measures: the Jaccard index and the area under ROC curve. The Jaccard index is a measure of overlap between two binary maps A and B , defined as the size of the intersection divided by the size of the union of the sample sets:

$$J(A, B) = \frac{|A \cap B|}{|A \cup B|}.$$

It is test-dependent: changing the risk or the multiple comparisons correction at the estimation step will change the obtained network shape, modifying Jaccard index. That is why, we also computed classical ROC curves and measured corresponding Areas Under Curve.



Validation and Results

We first checked how the obtained networks corresponded to the expected networks, those where the used seed was

placed. As shown in fig. 19, all the considered seeds have their best scores with the expected reference, and all six functional networks were considered sufficiently well detected. Results with ROC curves will not be shown here, but were always consistent.

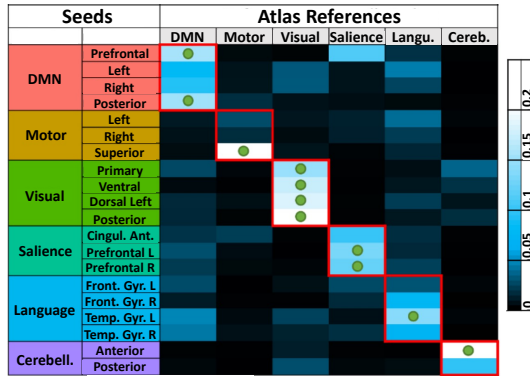


Figure 19: Colormaps of median Jaccard indices for all pairs of seeds and MSDL references. Green circles: successful detections (Jaccard > 0.1).

Fig. 20 shows the evolution of the detected DMN for one subject and one seed, according to the acquisition time. With a 2 min long acquisition, the detected map is mainly noise. From 4 min to 12 min, the false positive noise has disappeared while the frontal component of the DMN starts growing and the posterior starts being detected. After 14 min, DMN detection is good and, more interestingly, stable. This plateau is also reflected in the performance scores, and is observed in every subject, as shown in fig. 21.

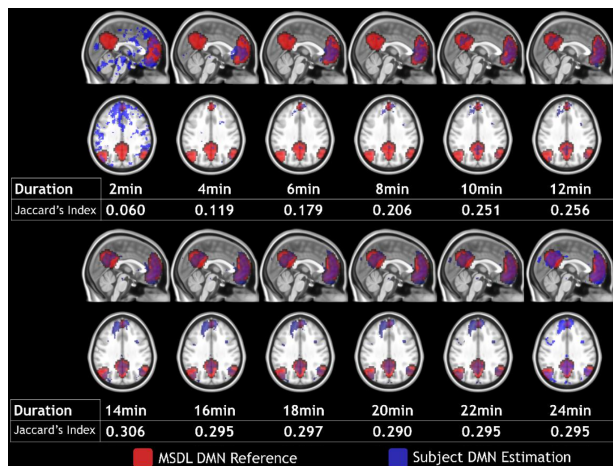


Figure 20: Evolution of Jaccard indices with respect to acquisition time for a DMN estimation (blue) compared to MSDL DMN (red), for one subject and one seed.

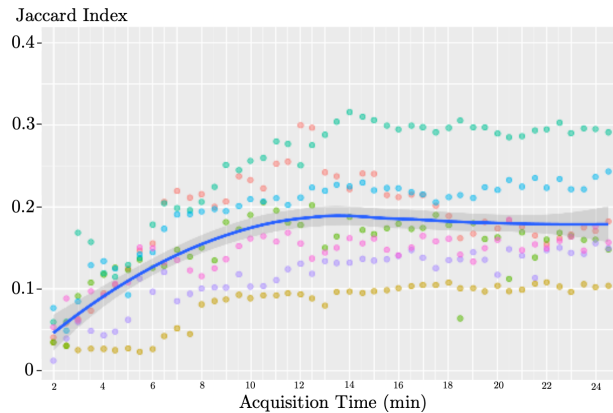


Figure 21: DMN: Jaccard indices evolution according to acquisition time. Each color corresponds to a subject. Blue line: local non-parametric regression (LOESS).

This phenomenon of quality stabilization after a certain acquisition time is also observed for the other networks studied. As shown in fig. 22, for all networks, a fast increasing score followed by a stabilization stage can be observed on the LOESS curves. A good compromise between score stabilization and acquisition length seems to be reached around between 12 min and 16 min.

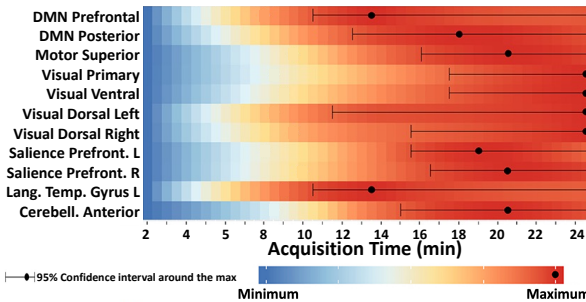


Figure 22: Colormaps of Jaccard indices according to acquisition time for all selected reference/seed pairs. Each line corresponds to the computation of one LOESS curve.

Take-Home Message

- The estimated functional networks stabilize after a certain acquisition time.
- For our set of sequence parameters, we suggest 14 min (240 volumes) as a good compromise.

Main Related Publications: [106, 107, 105]

2

Joint EEG-fMRI neurofeedback

Neurofeedback (NF) consists in presenting a subject with a stimulus directly related to his or her current brain activity. It can be used to teach subjects to regulate their own brain functions by providing real-time sensory feedback. NF is a rapidly growing field of research and has shown promise in treating a variety of neural pathologies [14]. For example, after a stroke, motor recovery is generally quite limited after one year [61]. Changes may have occurred, leading to significant functional reorganization of the motor network, sometimes even in cortical areas distant from the focal lesion [50]. NF has the potential to induce adaptive neural plasticity by selecting specific patterns and thus contribute to restore lost motor function [111, 118].

Although Electroencephalography (EEG) is currently the main modality used by NF clinical practitioners, it lacks specificity due to its low spatial resolution. Research has therefore recently turned to other modalities that more precisely target the activity of different brain regions. Thus, dynamic research into functional fMRI-NF holds promise for the treatment of depression [120, 43], chronic pain and stroke [64, 119], as it offers real-time imaging of activity in deep brain structures with high spatial resolution. However, the low temporal resolution and high costs and constraints associated with operating fMRI-NF limit the development of many applications. While promising, current NF technologies suffer from that antagonism between high (fMRI) and low (EEG) burden solutions. The future belongs to hybrid answers that combine the best of both approaches.

In the last years, the Empenn team led the Hemisfer¹ project to develop a hybrid EEG-MRI neurofeedback platform. Figure 23 shows the different steps of such an acquisition: the MRI-compatible EEG cap is installed, the subject is then positioned in the MRI, and a screen displays the visual feedback.

¹<https://team.inria.fr/empenn/research/scientific-activities/hemisfer-projects/>



Figure 23: Reproduced from Mathis Fleury's thesis: preparation of a simultaneous EEG-MRI-NF session with a 3T MRI and a 64 electrodes EEG cap, at the Neurinfo imaging platform. (a) Installation of the EEG subsystem and verification of impedance outside the MR environment, (b) Installation of the MR coil and rechecking of the EEG impedance, (c) Placement of the amplifiers, battery and LCD screen to display the visual feedback.

Figure 24 describes the developed framework: during simultaneous EEG-MRI acquisition, a real-time processing is computing two scores, one from EEG and the other from fMRI, depending on the targeted cerebral area. These two scores are combined in a visual feedback presented to the subject, to potentially reward him/her for having accomplished the desired task.

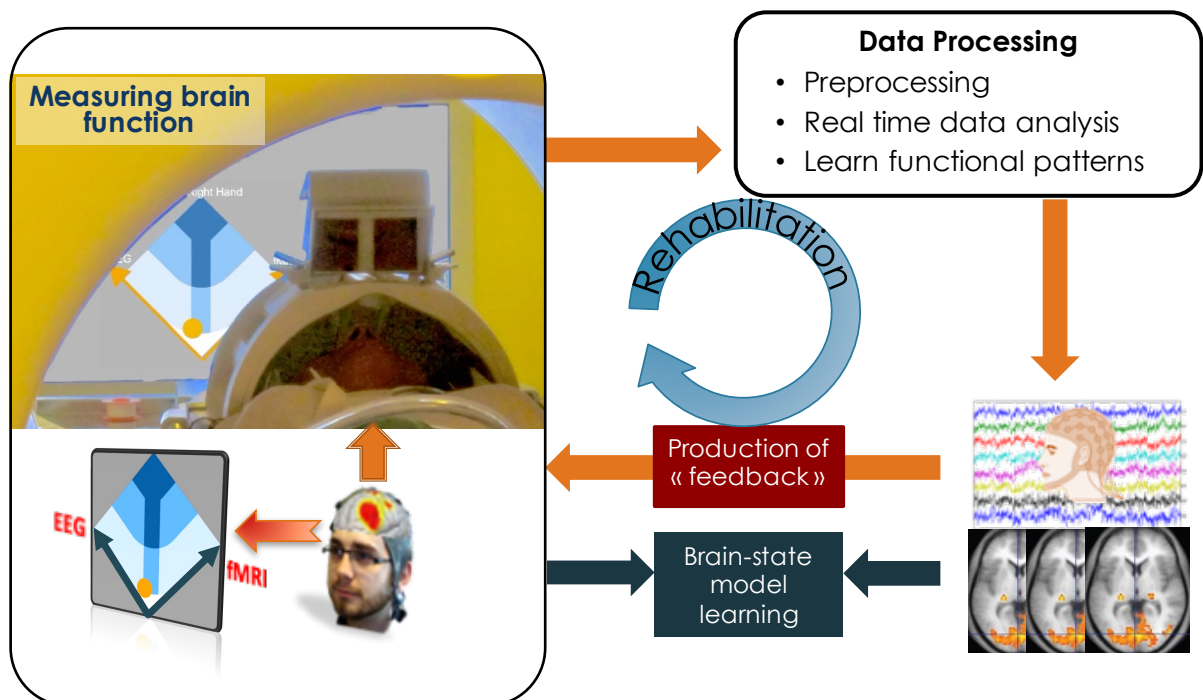


Figure 24: Hybrid EEG-MRI neurofeedback platform for stroke rehabilitation (Hemisfer project)

Finally, figure 25 presents two bimodal neurofeedback metaphors, investigated in the Hemisfer project [88], as well as two time series of the NF scores, computed in real-time. The main idea is to take advantage of the characteristics of the two modalities, EEG and fMRI, which are very complementary, even if they do not measure the same type of signal. Indeed, fMRI has an excellent spatial resolution, of the order of a millimeter, and a lower temporal resolution, of the order of a second, whereas EEG has a high temporal resolution (milliseconds), but a lower spatial resolution. The combined use of these two modalities for an NF protocol had so far only been explored by another group, Zotev and colleagues [120].

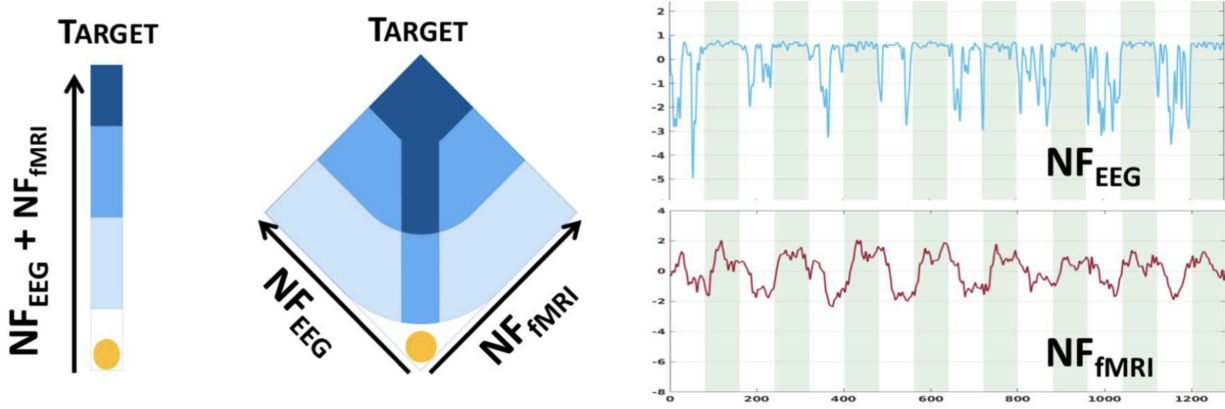


Figure 25: Bimodal neurofeedback metaphors (1D on the left, 2D on the middle) displayed during neurofeedback sessions [88]. 1D: the ball position represents the sum of the two neurofeedback scores, from EEG and from fMRI. 2D: the left and right axes represent respectively the EEG and fMRI scores. In both cases, the subject's goal is to bring the ball into the dark blue area. The two plots on the right show NF scores from EEG and from fMRI; green areas are task and white areas are rest.

This ambitious project, in collaboration with the Hybrid and Panama Inria teams and involving clinicians, aimed at taking full advantage of the NF paradigm in the context of rehabilitation and psychiatric disorders. Functional and metabolic information from fMRI on the one hand and EEG on the other hand are combined to enhance the NF protocol. The NF-EEG-MRI hybrid platform is now fully operational and two clinical studies are underway or in preparation: on stroke and depression patients. This new multimodal procedure, exploiting the qualities of each of the modalities involved, requires new data processing tools and opens the door to very interesting methodological developments.

In the following sections, I will present some of our contributions in this area over the past few years: electrodes detection during simultaneous EEG/fMRI acquisitions, multimodal EEG and fMRI source estimation using sparse constraints, and a sparse EEG-informed fMRI model for hybrid EEG-fMRI neurofeedback prediction. Each of them will be synthesized on a double page and the interested reader can refer to the publications listed at the end of the pages for more details. The figures presented are generally extracted from the above mentioned publications. These contributions are the result of two master internships I supervised, Mathis Fleury and Caroline Pinte, and three postdoctoral researchers with whom I collaborated with: Thomas Oberlin, Saman Noorzadeh and Claire Cury.

Electrodes Detection During Simultaneous EEG/fMRI

Context As mentioned in the introduction, electroencephalography (EEG) and functional MRI (fMRI) are two complementary modalities that show promise in the context of neurofeedback. Indeed, fMRI has an excellent spatial resolution, in the order of a millimeter, and a lower temporal resolution, in the order of a second, while EEG has a high temporal resolution (milliseconds), but a lower spatial resolution. In fact, source localization in EEG requires the solving of an inverse problem that is sensitive to several parameters [85], one of the main ones being the forward head model used. Another important parameter for the inverse problem is the 3D position of the electrodes on the scalp [3]. Indeed, the accuracy of the estimated coordinates of the EEG electrodes impacts the localization of the EEG sources. Position errors lead to inaccuracies in the estimation of the EEG inverse solution [58]. This is an even more important issue in our case, involving simultaneous EEG/fMRI acquisitions, where several sessions and thus several EEG cap installations are required. Furthermore, in order to take full advantage of these mixed acquisitions, the registration between EEG and MRI data must be optimal. It is therefore essential to be able to obtain the EEG electrode positions reliably and accurately.

In this context of simultaneous EEG-MRI acquisitions, an external measurement instrument, MRI, is available and seems natural. However, one difficulty is that MRI-compatible EEG systems are specifically designed to be as invisible as possible on most MRI sequences to minimize the presence of magnetic artifacts. Methods requiring manual measurements [32] or specific equipment [2, 112] have therefore been proposed. More recent studies have proposed the use of an Ultra-Short Echo-Time (UTE) sequence in which the electrodes are more visible [22, 69]. This type of recently proposed sequences [53, 57] allows to visualize the tissues with a very short T2 and T2*, such as cortical bone, tendons and ligaments, and has the side effect of enabling the imaging of MR compatible electrodes. The introduction of these new sequences opens the door to new methods, more automatic and

more easily usable in the clinical routine. Indeed, no additional equipment is required, and the additional acquisition time is quite short, which does not overburden the corresponding EEG-fMRI studies.

Contribution We proposed two methods to automatically detect the position of EEG electrodes from a UTE MRI sequence. In the first work [40], a segmentation step followed by a Hough transform provided a set of candidate positions, then an EEG cap model was registered on this set of detections to select the right number of electrodes. As our number of available data increased, we then replaced the first step by a machine learning based one [89].

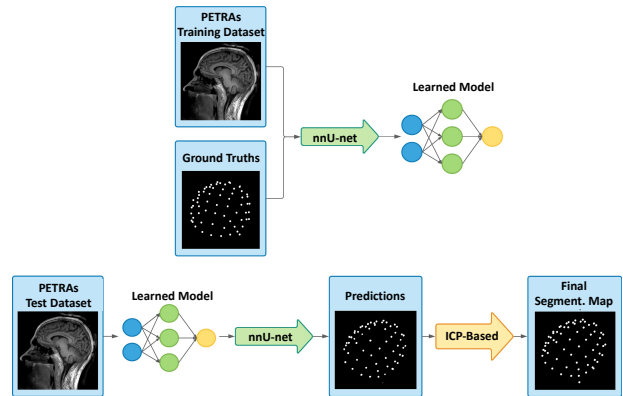


Figure 26: Overview of the detection framework. Learning process (top), Deep learning-based prediction and Registration-based refinement step (bottom).

Therefore, as illustrated in fig. 26, we proposed a new two-fold approach based on a combination of deep learning and template-based registration. In fact, our method starts by training a model to detect the position of the electrodes in a MRI volume. This model is based on the U-Net neural network, a fully convolutional neural network whose architecture allows to obtain accurate segmentations [94]. As mentioned above, we use a type of UTE sequence: the PETRA (Pointwise Encoding Time reduction with Radial Acquisition) sequence [51], which is gradually becoming the new standard in applications of

UTE sequences. An example of this type of images is shown in fig. 27. The electrodes are only visible on the PETRA. Finally, we use the Iterative Closest Point (ICP) [13] algorithm to take into account the geometrical constraints after the deep learning phase, and to obtain labeling of the electrodes.

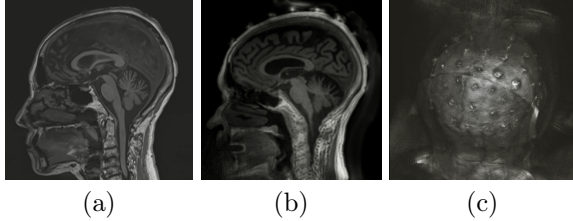


Figure 27: Example of images: (a) T1, (b) PETRA, (c) Volume Rendering of the PETRA image.

To train our model and validate our method, a ground truth was manually created for each PETRA volume, in the form of labeled segmentation maps with same dimension as PETRA images. The training dataset thus consists of 37 PETRA images, and their associated ground truth and we used the 3D U-Net [26] network. Once the model is trained, predictions are made on the test dataset (23 new PETRA volumes). To reinforce the strong geometrical *a priori* on the relative electrodes positions, we proposed a second step improving the neural network predictions. The main objectives are to force the number of detections to be exactly equal to 65, and to correctly label the electrodes. As illustrated in fig. 28, the n detections (n is not necessarily equal to 65) are registered on an average EEG cap model, using the ICP algorithm. This registered template is then used to remove outliers and retrieve missing electrodes.

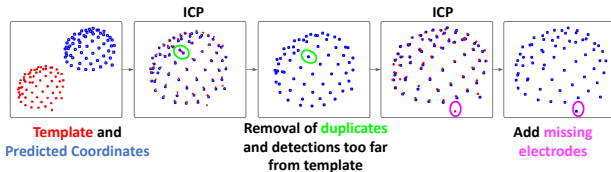


Figure 28: Description of the ICP-based refinement step.



Validation and Results

The robustness brought by the ICP step allowed us to remove the classical test-time augmentation phase, in order to accelerate the prediction time of the neural network. Finally, on our setup and for one PETRA volume, the learned neural network provided its predictions

in about 2 min, while the ICP-based refinement step took place in a few seconds. The main detection results on the test dataset are provided in table 2. The intermediate results of the neural network are also shown, justifying the interest of the refinement step.

	Deep learning detection	Final results
Position Error (mean \pm std in mm)	6.78 ± 25.4	2.23 ± 1.4
PPV (%)	96.3	99.8
#Labeling Errors mean (max)	3.2 (13)	0 (0)

Table 2: Row 1: mean and standard deviation values of Position Error. Row 2: Positive Predictive Value. Row 3: Number of labeling errors among the true positives.

100% of the electrodes were correctly labeled in our final results. As shown in the table, this was not the case after the deep learning step. We cannot always rely on the labeling of intermediate results. Indeed, the number of labeling errors can be as many as 13 in a volume. In fact, these observed errors often correspond to a simple offset in labeling: an electrode is incorrectly labeled and all its neighbors are then likely to be contaminated by this error. We therefore decided to disregard the labeling information provided by the neural network and rely solely on the ICP result for this. It may seem a bit odd to include labels in the ground truth for the training step, since we discard the resulting label afterwards. Nevertheless, our experiences have interestingly shown that training a neural network with labeled ground truth improves detection results (in term of position error) compared to a situation where the ground truths are simple binary maps. In particular, in the case where 65 different labels are provided during training, the network is more likely to detect a number close to 65 also during the test phase.

Take-Home Message

- Ultra-short TE sequences allow to visualize MRI-compatible EEG electrodes
- Our method uses deep learning and ICP to give excellent detection results

Main Related Publications: [42, 40, 89]

Multimodal EEG and fMRI Source Estimation

Context During neurofeedback sessions, the real-time constraint prevents the reconstruction of neural sources by solving the inverse problem associated with the EEG data. However, an *a posteriori* study of the localization of these sources would provide valuable information on the brain areas involved in the neurofeedback task. As mentioned in the previous section, the localization of the active electric sources from EEG requires solving an ill-posed inverse problem [109, 11]. One of the major challenges in the context of simultaneous EEG-MRI acquisition is therefore to take advantage of the good temporal resolution of the EEG on the one hand, and the good spatial resolution of the fMRI on the other hand.

These complementary strengths that these two modalities can provide, have stimulated a variety of studies [95]. These methods can be fMRI-constrained, or EEG-informed, when models driven on one modality act as the spatial (or temporal) prior on the solutions of the other modality [20, 7]. EEG and fMRI can also be used in symmetrical approaches, so that the information fusion is based on both data at the same time. Joint Independent Component Analysis [81] or Bayesian approaches [35] can be used to analyze both data in a joint space. According to the literature, the relation of neuronal activity, hemodynamics, and fMRI is still unclear [66]; however, the existing methods model this relationship based on the balloon model or neural mass models [6]. Although the integration of these two modalities has been studied a lot, it is mainly validated only on simulated data.

Contribution In [84, 83], we presented a multimodal approach to estimate the brain neuronal sources based on EEG and fMRI. Combining these two modalities can lead to source estimations with high spatio-temporal resolution. Our joint method is based on a first step where each of the data modalities are first modeled linearly based on the unknown sources. Afterwards, they are integrated in a joint framework which also add a constraint on the sparsity of sources.

As shown in fig. 29, in our model, the EEG and

fMRI signals, E and B , are linearly related to a matrix S of spatio-temporal sources, which we want to estimate. S has l rows and t_e columns, where l is the number of sources (space) and t_e the number of EEG samples (time). Classically each models relies on a matrix modeling the generation of each signal: the $j \times l$ leadfield matrix, G , where j is the number of electrodes, and the H matrix, containing shifted versions of the hemodynamic response.

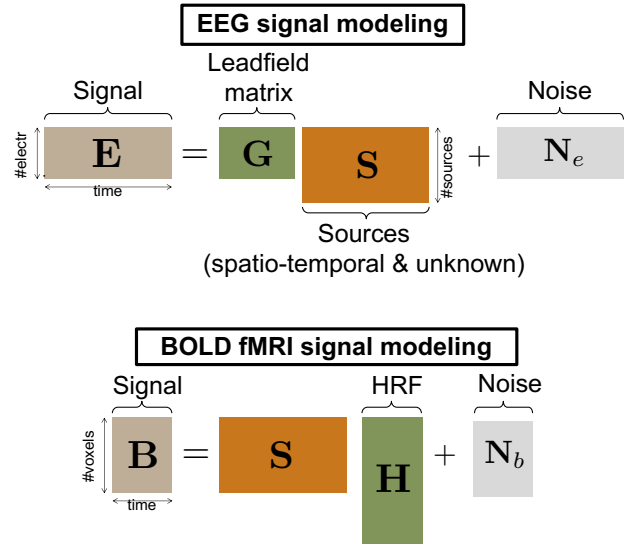


Figure 29: EEG and fMRI signal modeling. Our objective is to estimate S , the matrix of spatio-temporal sources at the origin of the two signals.

For each of this model, an underdetermined inverse problem must be solved to estimate S . The EEG inverse problem is ill-posed because EEG has much fewer channels than the number of sources ($l \gg j$). The fMRI is also ill-posed, this time because the sampling time is much less than the target temporal resolution of the source. We proposed a joint framework, combining the two inverse problems, to take advantage of the characteristics of each signal. In our joint modeling, a sparsity constraint is imposed on the source, via the \mathcal{L}_1 norm (in [84], other penalty terms are investigated on simulated data). Finally,

the sources can be estimated as:

$$\hat{\mathbf{S}} = \arg \min_{\mathbf{S}} \left\{ \alpha \|\mathbf{GS} - \mathbf{E}\|_2^2 + (1-\alpha) \|\mathbf{SH} - \mathbf{B}\|_2^2 + \lambda \|\mathbf{S}\|_1 \right\}. \quad (3)$$

$\alpha \in [0, 1]$ is a parameter adjusting the relative importance of EEG and fMRI in the source estimation. λ is a positive parameter weighting the sparsity constraint against the data-fidelity terms. Eq. (3) can be solved using a proximal algorithm such as the iterative soft thresholding [10]. The two data-fidelity terms have no reason to be of the same order of magnitude, so the α parameter can be difficult to adjust. In [83], we proposed a preliminary calibration step to normalized each term based on unimodal data.

Validation and Results

After validation on simulated data, we recorded simultaneous EEG and fMRI from 8 healthy subjects while doing a motor task of repeatedly clenching the right hand. The quality of a sources estimation was therefore evaluated by measuring the power of these sources in the left motor cortex, relative to the power in the rest of the brain. Fig 30 illustrates the effect of the proposed calibration step. Interestingly, after normalizing each data-fidelity term, the optimal α is not far from 0.5, which corresponds to an equal contribution from EEG and fMRI.

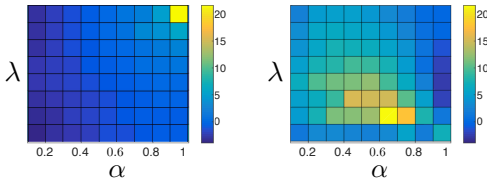


Figure 30: Performance scores for different parameter values, α and λ , without and with the calibration step introduced in [83].

Fig. 31 compares the estimated activations in the left and right motor cortex for the proposed method and for unimodal estimations ($\alpha = 0$ and $\alpha = 1$). The observed difference is bigger in the joint reconstruction, suggesting an activation pattern more consistent with the task performed.

The spatial result for a subject is illustrated in fig. 32. The fMRI-based method shows increased activity in the left motor cortex and precise localization of active areas (SMA and M1), whereas EEG detected activity in the SMA but not in the left motor

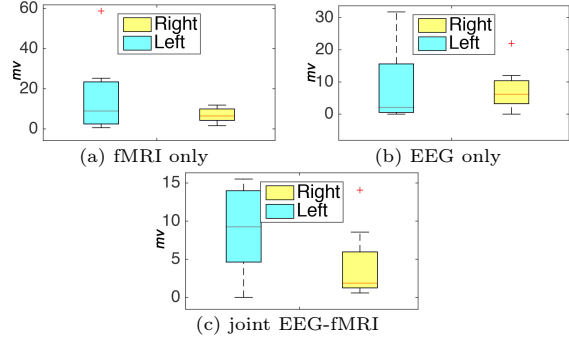


Figure 31: Box plots over eight subjects of the activations power in the union of the premotor and primary motor regions in both hemispheres, while right-hand motor task.

cortex. Furthermore, in both of these unimodal results, activations were detected in areas not involved in the task. The multimodal approach seems capable of avoiding the false positives of the unimodal approaches, and has detected high activities in both SMA and M1.

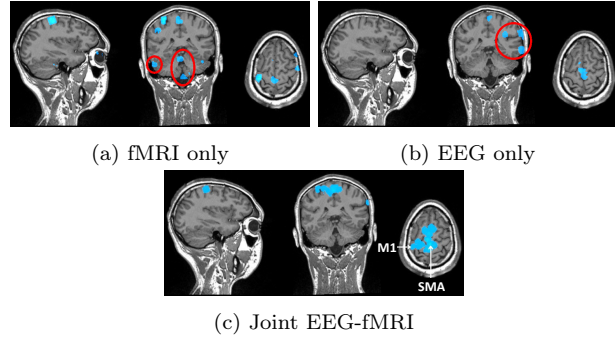


Figure 32: Estimated location of sources. Blue zones: active sources shown according to their power score. Red circles: Unexpected detections of activation.

Take-Home Message

- Sparsity constraint helps to solve ill-posed EEG/BOLD inverse problems.
- Symmetric EEG-fMRI joint reconstruction improves the source localization, even with a simple linear model.
- The temporal reconstruction has not yet been validated.

Main Related Publications: [84, 83]

Prediction of Multimodal Neurofeedback Scores from EEG



Context

As mentioned earlier, using simultaneously fMRI and EEG for multimodal neurofeedback sessions is very promising to design brain rehabilitation protocols. Indeed, offering real-time imaging of activity in deep brain structures with high spatial resolution, fMRI brings real added values to NF protocols. However using fMRI is costly, exhausting and time consuming, and cannot be repeated too many times for the same subject. For example, and for these reasons, the experimental protocol developed within the Hemisfer project for the rehabilitation of stroke patients alternates EEG-fMRI neurofeedback sessions and EEG sessions alone.

During the past few years, simultaneous EEG-fMRI recording has been used to understand the links between EEG and fMRI in different states of brain activity and has received recognition as a promising multimodal measurement of brain activity [1, 88]. Both modalities are sensitive to different aspects of brain activity with different speeds. EEG provides a direct measure of the changes in electrical potential occurring in the brain in real time, while fMRI indirectly estimates brain activity by measuring changes in the BOLD signal, reflecting neuro-vascular activity, which occurs, in general, a few seconds after a neural event [45, 66]. Several studies have investigated correlations between EEG signal and BOLD activity in specific and simple tasks [33, 97, 68] and have found different relationships of certain frequency bands of the EEG signal. All those studies reveal the existence of a link between EEG and fMRI, but this relationship varies considerably with the task, location in the brain, and frequency bands considered.



Contribution

In our context of multimodal EEG-fMRI neurofeedback, building on these unique data, we are interested in enriching the neurofeedback stimuli presented to patients in EEG-only sessions using a model learned in the mixed sessions. The original contribution of [29] concerns the prediction of multimodal NF scores from EEG recordings only, using a training phase where both EEG and fMRI synchronous signals, and therefore neuro-

feedback scores, are available. Fig. 33 describes the general framework of the method.

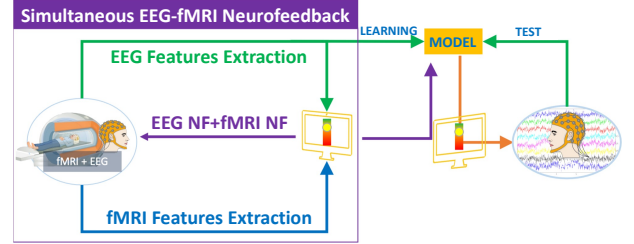


Figure 33: Description of the proposed framework to improve the EEG-only neurofeedback sessions by learning a model during EEG-fMRI sessions.

First, to extract relevant information from EEG data, a design matrix $\mathbf{X}_0(t) \in \mathbb{R}^{E \times B}$ is built, for each time t . E is the number of electrodes and B a number of frequency bands (10 bands between 8 Hz and 30 Hz, 3 Hz wide with an overlap of 1 Hz). $\mathbf{X}_0(t)$ contains a frequency decomposition of the past 2 s of the raw EEG signal. There is no linear relationship between the BOLD signal and the average power on frequency bands from the EEG signal. Therefore, to better match NF scores, we decided to apply a non-linear function to X_0 , classically used in fMRI to model BOLD signals [63], the canonical Hemodynamic Response Function (HRF). \mathbf{X}_0 is convolved on its temporal dimension with different HRF corresponding to different delays. Finally three new design matrices, \mathbf{X}_3 , \mathbf{X}_4 , and \mathbf{X}_5 are obtained, with respectively peak locations of 3, 4, and 5 s. These design matrices are then concatenated: $\mathbf{X}_c = [\mathbf{X}_0, \mathbf{X}_3, \mathbf{X}_4, \mathbf{X}_5]$.

During the training phase, corresponding to simultaneous EEG-fMRI acquisitions, reference fMRI neurofeedback scores $y_f(t)$ are available. The objective of the training is therefore to estimate an α such that

$$y_f(t) \approx \langle \mathbf{X}_c(t), \alpha \rangle = \sum_{i=1}^{4E} \sum_{j=1}^B X_{i,j} \alpha_{i,j}.$$

α can then be estimated by solving the following optimization problem:

$$\hat{\alpha} = \arg \min_{\alpha} \left[\sum_{t=1}^T \frac{1}{2} (y_f(t) - \langle \mathbf{X}_c(t), \alpha \rangle)^2 + \phi(\alpha) \right] \quad (4)$$

where ϕ is a regularization constraint on α , used to incorporate our *a priori* on the activation pattern of the NF-predictor. It has to: (i) be spatially sparse to regulate the model, as EEG signals are noisy, and to select the most relevant electrodes on each frequency bands; (ii) be smooth across different overlapped frequency bands; (iii) allow non-relevant frequency bands to be null. For all these reasons, we choose to use a $\mathcal{L}_{2,1}$ mixed norm (conditions i and ii) followed by a \mathcal{L}_1 -norm (condition iii), according to the idea in [49].

$$\begin{aligned}\phi(\alpha) &= \lambda \|\alpha\|_{2,1} + \rho \|\alpha\|_1 \\ &= \lambda \sum_m \sqrt{\sum_b \alpha_{m,b}^2} + \rho \sum_{m,b} |\alpha_{m,b}|\end{aligned}$$

Eq. (4) can be solved using the Fast Iterative Shrinkage Thresholding Algorithm (FISTA) [10], and we introduced a cross-validation-based process to determine the important λ parameter (ρ is fixed and constant across subjects and sessions).

Validation and Results

To test and validate our training framework, we used the data of 17 healthy subjects, scanned during simultaneous EEG-fMRI neurofeedback acquisition [65]². They all underwent three NF motor imagery sessions of 320s each, and the multimodal NF score was recorded: EEG score, y_e , was computed from the Laplacian operator centered around the motor region, and fMRI score, y_f was computed from the maximal intensity of BOLD signal covering the right-hand motor area and the Supplementary Motor Area (SMA).

For each subject, we considered one session as a learning set, and the two others as testing sets. Thus, one model α was learned per subject. Fig. 34 presents the correlation between our prediction and the original scores. As can be seen on the left of the figure, on the training set, it is possible to predict the fMRI score using only the EEG signal, with good correlation. During the testing, it can be noted that the bimodal score constructed using our prediction is more correlated to the ground truth bimodal score, than the EEG score alone. In fig. 35, examples of such scores are represented as time-series.

Finally, a strength of our model is the interpretability of the α obtained. Its sparsity and activation patterns can be studied and displayed (not shown here),

²Data available here: <https://openneuro.org/datasets/ds002338>

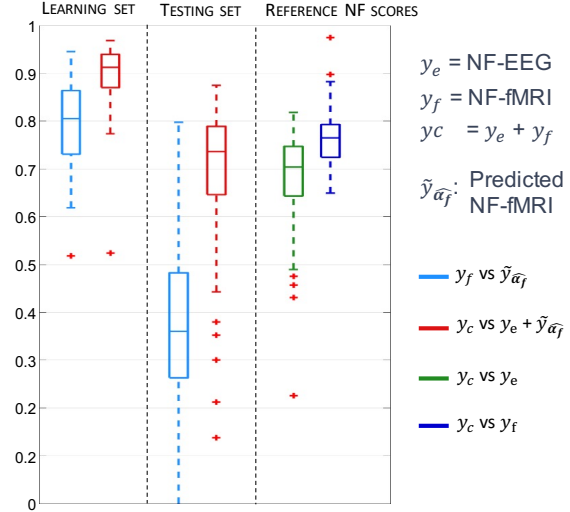


Figure 34: Pearson Correlation: in cyan, between our prediction of the fMRI score and the original one; in red between the original bimodal score and the predicted one.

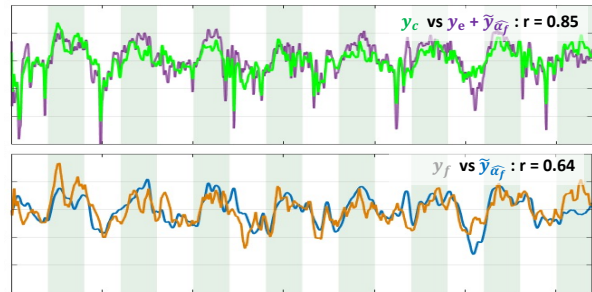


Figure 35: Examples of NF scores. The x-axis is the temporal axis. Vertical bands indicate the rest and task blocks. r is the correlation coefficient between each pair of time-series NF scores. (Top) correlation between the original bimodal score and our reconstructed one. (Bottom) Correlation between our predicted fMRI score and the original one.

indicating on which electrodes the learned model is mainly based to predict the fMRI score.

Take-Home Message

- fMRI neurofeedback score can be predicted using EEG signal only
- Promising results for clinical application: enhancing EEG-only sessions

Main Related Publications: [30, 28, 29]

3

Conclusions and Perspectives

In this manuscript I have tried to present the two facets of my interdisciplinary work with methods from applied mathematics and computer science and an application theme, related to the study of the brain in operation. I presented our main contributions on the topics of ASL perfusion imaging and hybrid EEG-fMRI neurofeedback. We have first introduced new image processing methods to improve the quality of images obtained from ASL acquisitions, but also original analysis methods of these images, in order to ease their use in a clinical setting. Indeed, individual studies, which allow conclusions to be drawn at the level of a single subject, are of increasing interest. Then, in the pioneering context of multimodal EEG-fMRI neurofeedback, we developed innovative and promising methodological frameworks, opening the door to improved neurofeedback brain rehabilitation, as well as to a better understanding of the links between the two modalities involved.

Many perspectives have been opened up on various themes, which I will address in a non-exhaustive manner in the following sections.

3.1 Arterial Spin Labeling Images Processing and Analysis

With the ASL acquisition technique now beginning to be well established and some degree of sequence homogenization having occurred, it is my belief that it is now time to look at more advanced applications of this quantitative perfusion information. I will list below some of the research directions that I believe are relevant, from the shortest to the longest term.

3.1.1 Multiparametric estimation

Cerebral Blood Flow (CBF) is not the only parameter of interest quantifiable with ASL. One other example is Arterial Transit Time (ATT), which provides information on the time it takes for blood to reach a given area of the brain. Several works have proposed to use specific sequences to estimate both CBF and ATT, often by varying the parameter TI (inversion time), thus allowing the classical Buxton model [23] to be fitted to estimate these parameters, see for example [47, 55]. More recent works [115, 114] have investigated the optimization of ASL MRI experiments. Interestingly, they demonstrated that a sequential multi-Post Labeling Delay (PLD) pseudo-continuous ASL protocol can be objectively optimized to maintain higher CBF accuracy across a wider range of ATTs than a single-PLD or evenly spaced multi-PLD protocol. An interesting question will be for example to seek, for a given acquisition time, the best compromise between the number of repetitions at a certain TI and the number of different TIs acquired. In [116], we started to look into that question (see figure 36), but a more thorough investigation is needed, for example using the powerful compressed sensing framework, as the acquisition at different TIs can be interpreted as a sampling scheme of the perfusion model.

On the other hand, the super-resolution method presented previously could also be used to generate high-resolution atlases of brain perfusion related parameters, such as CBF and ATT. We can imagine for example to introduce a non-local patch based *a priori* in the resolution of the kinetic model. As a matter of fact, current recommendations are generally to acquire a well resolved single-TI ASL series, and a low resolution multi-TI series to generate ATT maps [31]. However, the improvement of acquisition sequences combined with the application of a super-resolution algorithm, opens the door to the possibility of reconstructing more detailed images, which can provide information on a localized decrease or slowing of perfusion, not necessarily related to a global vascular territory. In addition, the generation of well-detailed ATT maps has the potential to allow the segmentation of these vascular territories, thus avoiding the need for specific sequence acquisitions. Indeed, in normal brains, the boundaries between different vascular territories have a longer ATT than their center. [38].

3.1.2 Functional connectivity estimation

Following our preliminary work on resting state ASL, the next step will naturally be to study the functional connectivity associated with the ASL data and to compare it with the connectivity obtained by the BOLD. In the medium term, an objective will be to provide new features and enhanced parametric maps of brain perfusion and mental state connectivity at rest, and to develop new analytical models of dynamic regional

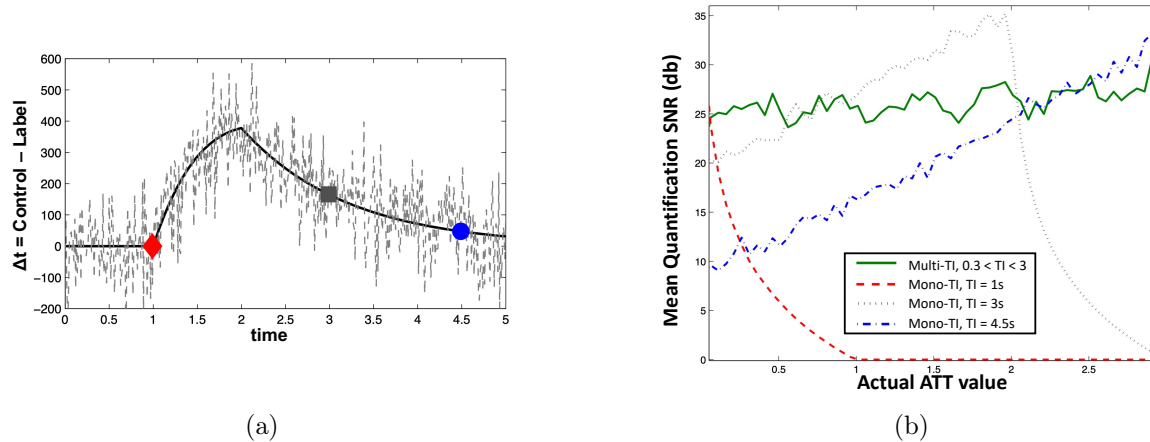


Figure 36: From [116]: (a) Example of the general kinetic model with labeling duration $\Delta t = 1$ s, Arterial Transit Time, $\text{ATT}=1$ s and $\text{CBF}= 10 \text{ mL}/(100\text{g})/\text{min}$ (dark solid curve) and its noisy version with average SNR 5dB (grey dashed curve). (b) Quality of CBF estimations: comparison between Mono-TI and Multi-TI (10 different TIs) methods for different actual ATT values. With mono-TI acquisition, as expected, the best CBF estimation is achieved when $\text{TI} \approx \text{ATT} + \Delta t$. On the other hand, as soon as $\text{TI} > \text{ATT} + \Delta t$, CBF starts to be severely underestimated. In contrast, multi-TI sampling provides stable quality.

perfusion. These advanced perfusion-derived functional models can be matched to structural models of connectomics features in order to infer indices of dynamic brain local perfusion from normal and pathological populations. From these maps, statistical descriptors can be derived to represent significant differences between groups of individuals. Furthermore, and as I will detail in the next section, these connectivity models could very well contribute to enrich a neurofeedback protocol, by defining more individualized rehabilitation targets.

3.1.3 Pediatric applications

In the longer term and in a more ambitious perspective, the consolidation of the foundations of ASL should open up a field of application in children, especially thanks to its non-invasiveness. In fact, the feasibility of ASL is beginning to be demonstrated for preterm and full-term infants [34], and has been the subject of several studies in the team [92, 24, 93, 91]. Therefore, we hope to extend these technical and methodological advances to even more challenging domains such as neonates and antenatal neurodevelopment. Although the link between cerebral blood flow and brain growth is not yet fully understood, one can make several hypotheses. As a matter of fact, some recent works [99] highlight a novel mode of neuronal migration that uses blood vessels as scaffolds. According to these studies, "astrocyte-vessel interaction is crucial during postnatal neuroblast migration" and this so-called "vasophilic migration plays also a role in recovery after stroke". In the same line, prenatal exposure to intermittent hypoxia (a condition where the tissues are not oxygenated adequately) has been shown [117] to delay neuronal migration which can cause abnormalities

in the brain growth. Introducing blood flow information in a biophysically based computational model of human brain growth, such as in [103], illustrated in figure 37, thus seems to be an interesting and promising research direction. A natural idea would be to locally adapt the overall brain growth factor to take into account the regional variation in cerebral blood flow. A region presenting an abnormal hypoperfusion will for example be growing slower than other normally perfused regions.

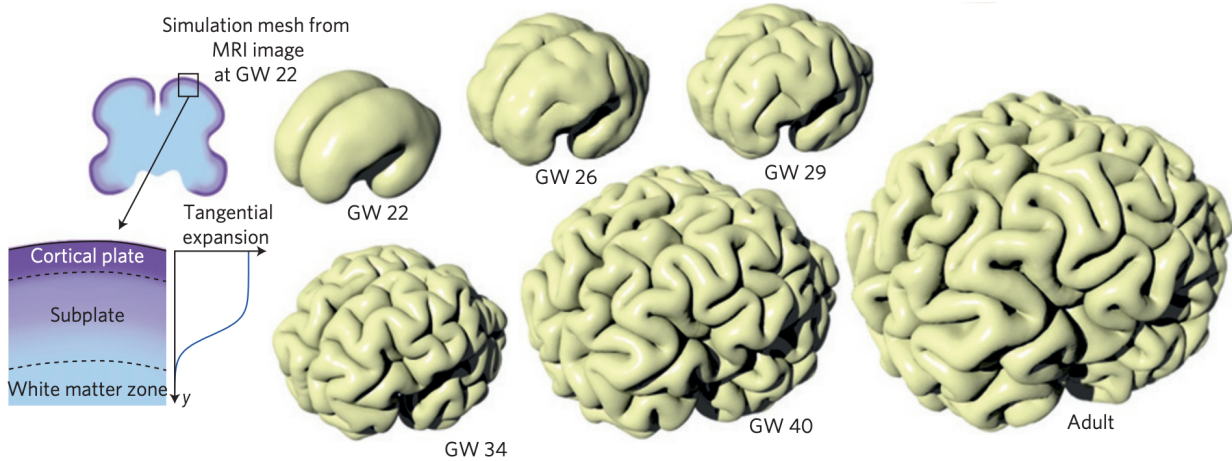


Figure 37: Reproduced from [103]: A simulation starting from a smooth fetal brain shows gyration as a result of uniform tangential expansion of the cortical layer. The brain is modeled as a soft elastic solid and a relative tangential expansion is imposed on the cortical layer as shown at left, and the system allowed to relax to its elastic equilibrium.

3.2 Portable and Personalized Neuro-Rehabilitation with Multimodal Neurofeedback

As mentioned, NF has shown promise in the treatment of a variety of neural pathologies, and multimodal EEG-fMRI NF can leverage both modalities to improve the quality of feedback and thus, potentially, the induced rehabilitation. Nevertheless, fMRI is a cumbersome and expensive modality, making it difficult to design personalized protocols. Recent developments in acquisition modalities and methodology open the door to more portable and personalized NF for easier and more efficient use in the clinic.

3.2.1 Personalized neurofeedback based on brain connectivity and graph signal processing

Brain connectivity studies the connections between different regions of the brain. Brain graphs or networks are powerful tools to model brain function or structure and have known an increasing success in neuroscience and related fields [9]. Under the natural assumption that functional brain information is related to the topology of the associated structural connectivity graph, Graph Signal Processing [101] is a research area that associates signals (i.e. brain activity) to an underlying brain network [19]. In the context of NF, we hypothesize that the study and modeling of brain networks will allow us to better understand the impact of NF-based rehabilitation and to better adapt them to the individual specificity of the brain architecture. The questions I would therefore like to address in the future are the following: Does the rehabilitation of stroke patients lead to a spatial reorganization of functional brain networks? How does this reorganization affect the improvement of clinical signs? Once this reorganization is better understood, how can it be taken into account to propose new NF protocols in order to better adapt them to each patient?

First, we could take advantage of the valuable data acquired within the Hemisfer project on stroke patients (5 EEG-fMRI NF sessions, 4 EEG-only sessions, over 5 weeks). Patients have preserved Cortico-Spinal Tract (CST), an ideal case for a first connectivity study of motor impaired patients, as the lesion did not severely impair the CST, leaving more room for local changes in brain functional connectivity. A natural first step would be for example to assess the changes induced by NF training on the organization of functional brain networks (by comparing the connectivity properties at the beginning and at the end of the NF protocol).

Based on these results, the goal would then be to identify novel NF targets that better correlate with successful rehabilitation outcomes (connectivity biomarkers). A key step in an NF protocol is to properly define and estimate a rehabilitation target according to which the intensity of the stimulus presented to the subject will be calculated. Most of NF literature assesses treatment effects focusing on behavioral outcomes and successful activation of targeted cortical regions. However, given the crucial role of large-scale networks reorganization for rehabilitation, it is now believed that assessment of brain connectivity is central to predict treatment response and to individualize rehabilitation therapies [8, 46]. Moreover, if NF protocols training connectivity strength between two specific brain regions have been designed [60], to the best of our knowledge, never a NF target based on individual structural connectivity has been proposed. An ambitious objective will thus be to propose new targets based on individual connectivity networks by using brain activity signals measured with EEG and functional MRI (BOLD or ASL), associated to individual structural networks estimated with diffusion imaging within the Graph Signal Processing framework.

3.2.2 Towards a more portable neurofeedback

Learning from multimodal EEG-fMRI neurofeedback sessions to enhance EEG-only sessions

Simultaneous EEG-fMRI provides more specific NF training [87]. However the use of the MRI scanner is more costly and less comfortable for patients as compared to EEG-only NF sessions. The methodological model presented above for learning information from mixed EEG-fMRI neurofeedback sessions to enrich EEG-only sessions is a first step towards more portable enhanced NF protocols. However, it now needs to be tested in a real-life situation. As a matter of fact, given the improved correlation of the proposed NF predictor with bimodal NF scores, it would be interesting to validate its improved performance in actual NF sessions compared to classical NF-EEG scores. In particular, to assess the response of subjects to the predicted bi-modal NF scores and especially the predicted NF-fMRI scores learned by the proposed model over a standard NF-EEG neurofeedback session, a new and large enough study is needed, as subjects can learn at different paces to regulate their own brain activity.

In addition, the final objective of this project is to learn from EEG-fMRI NF sessions in order to provide, outside the MRI scanner, improved NF-EEG sessions, whereas the current model has only been validated on EEG data acquired during simultaneous sessions (in order to have a ground truth). Future work will have to investigate the portability of the model learned on EEG-fMRI neurofeedback data, outside the MRI scanner, introducing new challenges, such as dealing with a different number of electrodes and the absence of ground truth once the EEG is measured outside the MRI scanner.

Functional near-infrared spectroscopy as an alternative to fMRI ?

The feasibility of using functional Near-Infrared Spectroscopy (fNIRS) in NF has recently been shown [39]. fNIRS is a noninvasive and portable optical neuroimaging technique that can detect changes in hemoglobin concentration associated with neural activity, similarly as with fMRI. Compared to fMRI and EEG, as illustrated in figure 38, fNIRS has both advantages and disadvantages. It offers better spatial resolution (between 2 and 3 cm) than EEG and potentially higher temporal resolution than fMRI, due to a higher sampling rate [59]. The practicality of the fNIRS is a major advantage over fMRI: it is easier to use, portable, safe, almost silent, and inexpensive. In addition, fNIRS acquisitions are less sensitive to head movements than EEG and fMRI. This makes it possible to use in more natural environments, for example by interacting with the subject. Furthermore, it allows the study of more specific populations for which fMRI acquisitions could be more complicated (e.g. stroke patients).

fNIRS is used to determine surface brain activities and can be easily coupled to an EEG cap to provide a portable EEG-fNIRS NF. Due to limitations in the power of light emitters, fNIRS cannot indeed be used to measure deep cortical activity, and has a lower spatial resolution than fMRI. This limits its use for NF protocols targeting the amygdala, such as in some psychiatric applications. Nevertheless, its high portability, as well as its compatibility with the EEG, make it an extremely promising modality for NF protocols targeting motor areas for example. Some recent studies [70, 56] have compared the use of fNIRS to EEG in the context of NF and have shown that the two modalities, although consistent, have different and complementary properties. This confirms our conclusions on the bimodal NF EEG-fMRI concerning the interest of combining the two measures of cortical activity: the electrophysiological and the hemodynamic responses. To the best of our knowledge, simultaneous EEG-fNIRS NF has never been investigated. Therefore, and always with the idea of lightening these rehabilitation protocols, the contribution of this new modality should be investigating

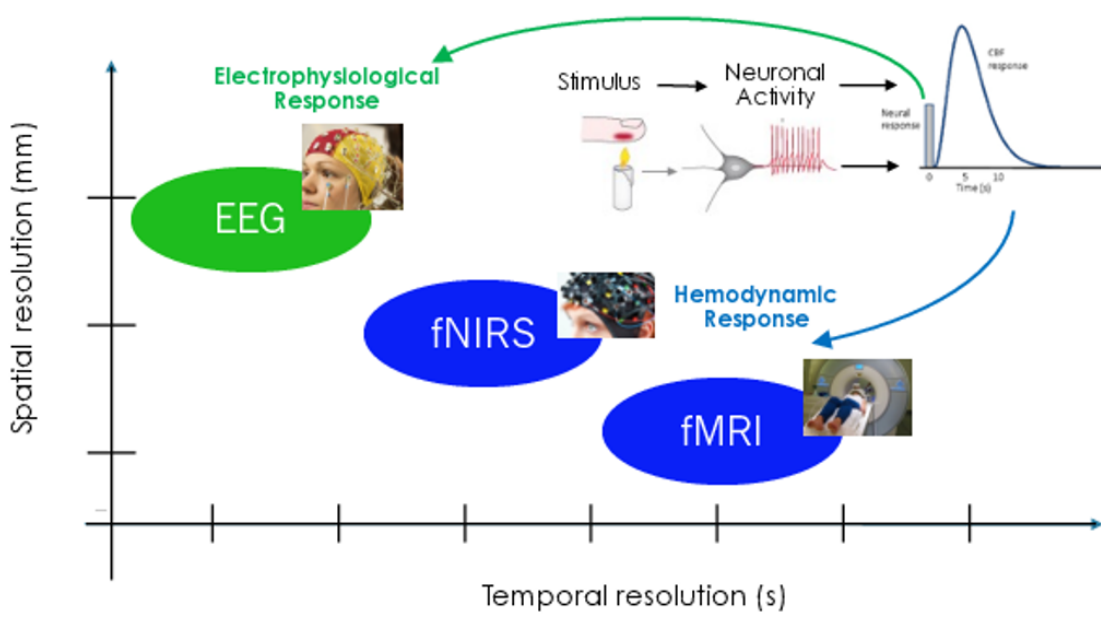


Figure 38: Characteristics of three modalities that can be used for neurofeedback: EEG, fNIRS, and fMRI. fNIRS and fMRI measure the hemodynamic response. fNIRS is a relatively “light” technique and appears to be a good compromise between the good temporal resolution of the EEG and its poorer spatial resolution on the one hand, and the good spatial resolution of fMRI and its poorer temporal resolution on the other.

to propose an EEG-fNIRS NF and compare it to the enhanced EEG-NF setting previously mentioned. As fNIRS shares some properties with fMRI, the integration of this new modality to EEG definitely has the potential to enable a portable and more specific NF training for patients.

Towards New Multisensory Neurofeedback

Current NF training usually provides basic visual feedback. Yet, the feedback is known to play a major role in NF or brain-computer interfaces [86, 67]. The feedback informs the user about the quality of his performance in real time to help him control his or her brain activity. Carefully selected feedbacks can reduce the time required by the user to learn to control the system and their own brain activity. In order to further develop NF protocols that can target a specific region or network, we can imagine to propose new NF feedbacks that will involve multisensory stimuli (e.g. visual, haptic, auditory). These feedbacks can be designed to activate brain regions specific to the considered pathology according in a rehabilitation scenario.

Our team already has experience in using a MR compatible vibrator for haptic stimulation of stroke patients [62]. As shown in figure 39, our group has also recently investigated the influence of virtual reality visual feedback on the illusion of movement induced by tendon vibration of the wrist in healthy participants [44, 41]. Indeed, haptic interfaces have the potential to improve performance and increase the pertinence of the feedback provided, particularly in the context of motor rehabilitation. The first results are

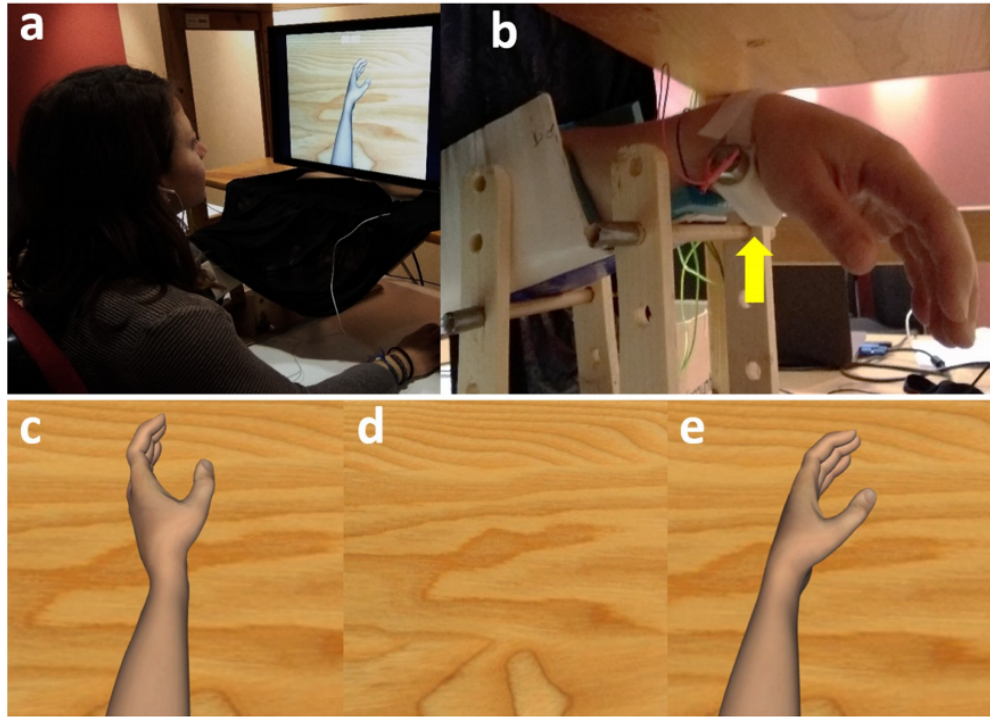


Figure 39: Description of the experimental prototype platform, developed by the Empenn and Hybrid teams and used in [44]. a-b) Set-up of the vibrator. A black curtain covered the forearm of the participant. c-d-e) Visualization of the three virtual visual conditions (respectively Moving, Hidden, Static condition).

promising and demonstrate the impact that these new multisensory neurofeedback methods could have in improving stroke rehabilitation. However, how to use these visuo-haptic systems, individually or in combination with other modalities, remains an open question that has not been thoroughly addressed by other groups.

To develop a methodological and experimental framework for implementing haptic-based NF, several questions remain thus open: 1) the mapping of NF information on the various available modalities, i.e., qualifying which NF features should be sent to which sensory modality and when, and 2) the adaptation/personalization of the sensory feedback depending for instance on the evolution of participant's results and/or on his/her personal characteristics (preference, personality traits, disability properties, etc).

Acronyms

- ASL** Arterial Spin Labeling. 7–18, 31–33, 36
- ATT** Arterial Transit Time. 7, 8, 32, 33
- BOLD** Blood Oxygenation Level Dependent. 18, 27–29, 33, 36
- CBF** Cerebral Blood Flow. 7, 8, 10–15, 18, 32, 33
- CST** Cortico-Spinal Tract. 35
- DMN** Default Mode Network. 18, 19
- DSC** Dynamic Susceptibility weighted Contrast. 11, 13, 15
- EEG** Electroencephalography. 1, 21–29, 31, 35–37
- fMRI** functional Magnetic Resonance Imaging. 1, 14, 18, 21–24, 26–29, 31, 35–37
- fNIRS** functional Near-Infrared Spectroscopy. 36, 37
- GLM** General Linear Model. 14, 16, 17
- HR** High Resolution. 12, 13
- HRF** Hemodynamic Response Function. 28
- ICP** Iterative Closest Point. 25
- M1** Primary Motor Cortex. 27
- MRI** Magnetic Resonance Imaging. 7
- NF** Neurofeedback. 21–23, 28, 29, 35–37
- PASL** Pulsed ASL. 13, 15
- pCASL** pseudo-Continuous ASL. 13, 18

PETRA Pointwise Encoding Time reduction with Radial Acquisition. 24, 25

PLD Post Labeling Delay. 32

RMSE Root-Mean-Square error. 13

ROC Receiver-Operating-Characteristics. 15, 17–19

rs-ASL Resting State ASL. 18

rs-fMRI Resting State fMRI. 18

SBA Seed Based Analysis. 18

SMA Supplementary Motor Area. 27, 29

SNR Signal-to-Noise Ratio. 10, 12, 14, 33

SR Super Resolution. 12, 13

TI Inversion Time. 8, 9, 32, 33

UTE Ultra-Short Echo-Time. 24, 25

Bibliography

- [1] Rodolfo Abreu, Alberto Leal, and Patrícia Figueiredo. Eeg-informed fmri: A review of data analysis methods. *Frontiers in Human Neuroscience*, 12, 02 2018.
- [2] P Adjamian, GR Barnes, A Hillebrand, IE Holliday, Krish Devi Singh, Paul Lawrence Furlong, E Harrington, CW Barclay, and PJG Route. Co-registration of magnetoencephalography with magnetic resonance imaging using bite-bar-based fiducials and surface-matching. *Clinical Neurophysiology*, 115(3):691–698, 2004.
- [3] Zeynep Akalin Acar and Scott Makeig. Effects of forward model errors on eeg source localization. *Brain topography*, 26, 01 2013.
- [4] David C. Alsop, John A. Detre, Xavier Golay, Matthias Gunther, Jeroen Hendrikse, Luis Hernandez-Garcia, Hanzhang Lu, Bradley J. MacIntosh, Laura M. Parkes, Marion Smits, Matthias J. P. van Osch, Danny J. J. Wang, Eric C. Wong, and Greg Zaharchuk. Recommended implementation of arterial spin-labeled perfusion mri for clinical applications: A consensus of the isrmr perfusion study group and the european consortium for asl in dementia. *Magnetic Resonance in Medicine*, 73(1):102–116, 2015.
- [5] J.S. Anderson, M.A. Ferguson, M. Lopez-Larson, and D. Yurgelun-Todd. Reproducibility of single-subject functional connectivity measurements. *American Journal of Neuroradiology*, 32(3):548–555, January 2011.
- [6] Abbas Babajani et al. Integrated MEG/EEG and fMRI model based on neural masses. *IEEE Transactions on Biomedical Engineering*, 53(9):1794–1801, 2006.
- [7] Andrew P Bagshaw et al. Analysis of the EEG–fMRI response to prolonged bursts of interictal epileptiform activity. *Neuroimage*, 24(4):1099–1112, 2005.
- [8] Danielle S. Bassett and Ankit N. Khambhati. A network engineering perspective on probing and perturbing cognition with neurofeedback. *Annals of the New York Academy of Sciences*, 1396(1):126–143, April 2017.
- [9] Danielle S Bassett and Olaf Sporns. Network neuroscience. *Nature Neuroscience*, 20(3):353–364, February 2017.
- [10] Amir Beck and Marc Teboulle. A fast iterative shrinkage-thresholding algorithm for linear inverse problems. *SIAM J. Imaging Sciences*, 2:183–202, 01 2009.
- [11] Hanna Becker et al. A performance study of various brain source imaging approaches. In *Int. Conf. on Acoustics, Speech and Signal Processing (ICASSP)*, pages 5869–5873. IEEE, 2014.

- [12] Christian F. Beckmann, Mark Jenkinson, and Stephen M Smith. General multilevel linear modeling for group analysis in fMRI. *NeuroImage*, 20(2):1052–1063, 2003.
- [13] P. J. Besl and N. D. McKay. A method for registration of 3-d shapes. *IEEE Transactions on Pattern Analysis and Machine Intelligence*, 14(2):239–256, 1992.
- [14] Niels Birbaumer, Ander Ramos Murguialday, Cornelia Weber, and Pedro Montoya. Chapter 8 neurofeedback and brain–computer interface. In *International Review of Neurobiology*, pages 107–117. Elsevier, 2009.
- [15] Rasmus M. Birn, Erin K. Molloy, Rémi Patriat, Taurean Parker, Timothy B. Meier, Gregory R. Kirk, Veena A. Nair, M. Elizabeth Meyerand, and Vivek Prabhakaran. The effect of scan length on the reliability of resting-state fMRI connectivity estimates. *NeuroImage*, 83:550–558, December 2013.
- [16] Bharat Biswal, F. Zerrin Yetkin, Victor M. Haughton, and James S. Hyde. Functional connectivity in the motor cortex of resting human brain using echo-planar mri. *Magnetic Resonance in Medicine*, 34(4):537–541, October 1995.
- [17] Ilaria Boscolo Galazzo, Silvia Storti, Alessandra Del Felice, Francesca Pizzini, Chiara Arcaro, Emanuela Formaggio, Roberto Mai, Michael Chappell, Alberto Beltramello, and Paolo Manganotti. Patient-specific detection of cerebral blood flow alterations as assessed by arterial spin labeling in drug-resistant epileptic patients. *PloS one*, 10:e0123975, 05 2015.
- [18] Sylvain Bouix, Sophia Swago, John D. West, Ofer Pasternak, Alan Breier, and Martha E. Shenton. “Evaluating Acquisition Time of rfMRI in the Human Connectome Project for Early Psychosis. How Much Is Enough?”. In Guorong Wu, Paul Laurienti, Leonardo Bonilha, and Brent C. Munsell, editors, *Connectomics in NeuroImaging*, Lecture Notes in Computer Science, pages 108–115, Cham, 2017. Springer International Publishing.
- [19] Abdelbasset Brahim and Nicolas Farrugia. Graph fourier transform of fMRI temporal signals based on an averaged structural connectome for the classification of neuroimaging. *Artificial Intelligence in Medicine*, 106:101870, June 2020.
- [20] Ted Brookings et al. Using ICA and realistic bold models to obtain joint EEG/fMRI solutions to the problem of source localization. *Neuroimage*, 44(2):411–420, 2009.
- [21] A. Buades, B. Coll, and J.-M. Morel. A non-local algorithm for image denoising. In *2005 IEEE Computer Society Conference on Computer Vision and Pattern Recognition (CVPR’05)*, volume 2, pages 60–65 vol. 2, 2005.
- [22] Russell Butler, Guillaume Gilbert, Maxime Descoteaux, Pierre-Michel Bernier, and Kevin Whittingstall. Application of polymer sensitive mri sequence to localization of eeg electrodes. *Journal of Neuroscience Methods*, 278:36 – 45, 2017.
- [23] Richard B. Buxton, Lawrence R. Frank, Eric C. Wong, Bettina Siewert, Steven Warach, and Robert R. Edelman. A general kinetic model for quantitative perfusion imaging with arterial spin labeling. *Magnetic Resonance in Medicine*, 40(3):383–396, 1998.

- [24] Domitille Cadiot, Romain Longuet, Bertrand Bruneau, Catherine Treguier, Aline Carsin-Vu, Isabelle Corouge, Constantin Gomes, and Maïa Proisy. Magnetic resonance imaging in children presenting migraine with aura: Association of hypoperfusion detected by arterial spin labelling and vasospasm on mr angiography findings. *Cephalalgia*, 38:033310241772357, 07 2017.
- [25] Gang Chen, Ziad S. Saad, Audrey R. Nath, Michael S. Beauchamp, and Robert W. Cox. fMRI group analysis combining effect estimates and their variances. *NeuroImage*, 60(1):747–765, 2012.
- [26] Özgün Çiçek, Ahmed Abdulkadir, Soeren S. Lienkamp, Thomas Brox, and Olaf Ronneberger. 3d u-net: Learning dense volumetric segmentation from sparse annotation. *CoRR*, abs/1606.06650, 2016.
- [27] Pierrick Coupé, José V Manjón, Maxime Chamberland, Maxime Descoteaux, and Bassem Hiba. Collaborative patch-based super-resolution for diffusion-weighted images. *NeuroImage*, page epub ahead of print, June 2013.
- [28] Claire Cury, Pierre Maurel, Rémi Gribonval, and Christian Barillot. Can we learn from coupling EEG-fMRI to enhance neuro-feedback in EEG only? In *OHBM 2019 - Annual Meeting Organization for Human Brain Mapping*, page 1, Rome, Italy, June 2019.
- [29] Claire Cury, Pierre Maurel, Rémi Gribonval, and Christian Barillot. A sparse EEG-informed fMRI model for hybrid EEG-fMRI neurofeedback prediction. *Frontiers in Neuroscience*, January 2020.
- [30] Claire Cury, Pierre Maurel, Giulia Lioi, Rémi Gribonval, and Christian Barillot. Learning bi-modal EEG-fMRI neurofeedback to improve neurofeedback in EEG only. In *Real-Time Functional Imaging and Neurofeedback*, pages 1–2, Maastricht, Netherlands, December 2019.
- [31] Weiying Dai, Tamara Fong, Richard Jones, Edward Marcantonio, Eva Schmitt, Sharon Inouye, and David Alsop. Effects of arterial transit delay on cerebral blood flow quantification using arterial spin labeling in an elderly cohort. *Journal of magnetic resonance imaging: JMRI*, 45, 07 2016.
- [32] Jan C de Munck, Petra J van Houdt, Ruud M Verdaasdonk, and Pauly PW Ossenblok. A semi-automatic method to determine electrode positions and labels from gel artifacts in eeg/fmri-studies. *Neuroimage*, 59(1):399–403, 2012.
- [33] J.C. de Munck, S.I. Gonçalves, L. Huijboom, J.P.A. Kuijser, P.J.W. Pouwels, R.M. Heethaar, and F.H. Lopes da Silva. The hemodynamic response of the alpha rhythm: An eeg/fmri study. *NeuroImage*, 35(3):1142–1151, 2007.
- [34] Jill B. De Vis, Esben T. Petersen, Linda S. de Vries, Floris Groenendaal, Karina J. Kersbergen, Thomas Alderliesten, Jeroen Hendrikse, and Manon J.N.L. Benders. Regional changes in brain perfusion during brain maturation measured non-invasively with arterial spin labeling mri in neonates. *European Journal of Radiology*, 82(3):538 – 543, 2013. Breast Imaging.
- [35] Thomas Deneux et al. EEG-fMRI fusion of paradigm-free activity using kalman filtering. *Neural computation*, 22(4):906–948, 2010.
- [36] Agnès Desolneux, L. Moisan, and J. Morel. A grouping principle and four applications. *IEEE Transactions on Pattern Analysis and Machine Intelligence*, 25(4):508–513, 2003.

- [37] J.A. Detre, J.S. Leigh, Donald S. Williams, and Alan P. Koretsky. Perfusion imaging. *Magnetic Resonance in Medicine*, 23:37–45, 1992.
- [38] Manus J Donahue, Eric Achten, Petrice M Cogswell, Frank-Erik De Leeuw, Colin P Derdeyn, Rick M Dijkhuizen, Audrey P Fan, Rashid Ghaznawi, Jeremy J Heit, M Arfan Ikram, Peter Jezzard, Lori C Jordan, Eric Jouvent, Linda Knutsson, Richard Leigh, David S Liebeskind, Weili Lin, Thomas W Okell, Adnan I Qureshi, Charlotte J Stagg, Matthias JP van Osch, Peter CM van Zijl, Jennifer M Watchmaker, Max Wintermark, Ona Wu, Greg Zaharchuk, Jinyuan Zhou, and Jeroen Hendrikse. Consensus statement on current and emerging methods for the diagnosis and evaluation of cerebrovascular disease. *Journal of Cerebral Blood Flow & Metabolism*, 38(9):1391–1417, 2018. PMID: 28816594.
- [39] Ann-Christine Ehlis, Beatrix Barth, Justin Hudak, Helena Storchak, Lydia Weber, Ann-Christin S. Kimmig, Benjamin Kreifelts, Thomas Dresler, and Andreas J. Fallgatter. Near-infrared spectroscopy as a new tool for neurofeedback training: Applications in psychiatry and methodological considerations. *Japanese Psychological Research*, 60(4):225–241, 2018.
- [40] Mathis Fleury, Christian Barillot, Elise Bannier, Marsel Mano, and Pierre Maurel. Automated Electrodes Detection during simultaneous EEG/fMRI. *Frontiers in information and communication technologies*, pages 1–15, 2018.
- [41] Mathis Fleury, Giulia Lioi, Christian Barillot, and Anatole Lécuyer. A survey on the use of haptic feedback for brain-computer interfaces and neurofeedback. *Frontiers in Neuroscience*, 14, 06 2020.
- [42] Mathis Fleury, Pierre Maurel, Marsel Mano, Elise Bannier, and Christian Barillot. Automatic Electrodes Detection during simultaneous EEG/fMRI acquisition. In *ISMRM 2018*, pages 1–3, Paris, France, June 2018.
- [43] Thomas Fovet, Renaud Jardri, and David Linden. Current issues in the use of fmri-based neurofeedback to relieve psychiatric symptoms. *Current pharmaceutical design*, 21, 06 2015.
- [44] Salomé Le Franc, Mathis Fleury, Mélanie Cogne, Simon Butet, Christian Barillot, Anatole Lecuyer, and Isabelle Bonan. Influence of virtual reality visual feedback on the illusion of movement induced by tendon vibration of wrist in healthy participants. *PLOS ONE*, 15(11):e0242416, November 2020.
- [45] K. J. Friston, P. Jezzard, and R. Turner. Analysis of functional mri time-series. *Human Brain Mapping*, 1(2):153–171, 1994.
- [46] Lioi Giulia, Veliz Adolfo, Coloigner Julie, Duché Quentin, Butet Simon, Mathis Fleury, Emilie Leveque-Le Bars, Elise Bannier, Anatole Lécuyer, Christian Barillot, and Isabelle Bonan. The impact of neurofeedback on effective connectivity networks in chronic stroke patients. May 2020.
- [47] J Gonzalez-At, David Alsop, and John Detre. Cerebral perfusion and arterial transit time changes during task activation determined with continuous arterial spin labeling. *Magnetic resonance in medicine: official journal of the Society of Magnetic Resonance in Medicine / Society of Magnetic Resonance in Medicine*, 43:739–46, 06 2000.

- [48] M Grade, Juan Antonio Hernández Tamames, Francesca Pizzini, Eric Achten, Xavier Golay, and Marion Smits. A neuroradiologist’s guide to arterial spin labeling mri in clinical practice. *Neuroradiology*, 57, 09 2015.
- [49] Alexandre Gramfort, Daniel Strohmeier, Jens Haueisen, Matti Hamalainen, and Matthieu Kowalski. Functional brain imaging with m/eeg using structured sparsity in time-frequency dictionaries. volume 22, pages 600–11, 07 2011.
- [50] Christian Grefkes and Nick Ward. Cortical reorganization after stroke: How much and how functional? *The Neuroscientist: a review journal bringing neurobiology, neurology and psychiatry*, 20, 06 2013.
- [51] David M. Grodzki, Peter M. Jakob, and Bjoern Heismann. Ultrashort echo time imaging using pointwise encoding time reduction with radial acquisition (petra). *Magnetic Resonance in Medicine*, 67(2):510–518, 2012.
- [52] Sven Haller, Greg Zaharchuk, David L. Thomas, Karl-Olof Lovblad, Frederik Barkhof, and Xavier Golay. Arterial spin labeling perfusion of the brain: Emerging clinical applications. *Radiology*, 281(2):337–356, 2016. PMID: 27755938.
- [53] Joanne E. Holmes and Graeme M. Bydder. Mr imaging with ultrashort te (ute) pulse sequences: Basic principles. *Radiography (London 1995)*, 11(3):163–174, 2005. RADIOLOGY AND NUCLEAR MEDICINE.
- [54] P.J. Huber. Robust estimation of a location parameter. *The Annals of Mathematical Statistics*, 1964.
- [55] Megan Johnston, Kun Lu, Joseph Maldjian, and Youngkyoo Jung. Multi-ti arterial spin labeling mri with variable tr and bolus duration for cerebral blood flow and arterial transit time mapping. *IEEE transactions on medical imaging*, 34, 01 2015.
- [56] Vera Kaiser, Günther Bauernfeind, Alex Kreilinger, Tobias Kaufmann, Andrea Kübler, Christa Neuper, and Gernot R. Müller-Putz. Cortical effects of user training in a motor imagery based brain–computer interface measured by fNIRS and EEG. *NeuroImage*, 85:432–444, January 2014.
- [57] V. Keereman, Y. Fierens, T. Broux, Y. De Deene, M. Lonneux, and S. Vandenberghe. MRI-based attenuation correction for PET/MRI using ultrashort echo time sequences. *Journal of Nuclear Medicine*, 51(5):812–818, May 2010.
- [58] Deepak Khosla, Manuel Don, and Betty Kwong. Spatial mislocalization of eeg electrodes – effects on accuracy of dipole estimation. *Clinical Neurophysiology*, 110(2):261 – 271, 1999.
- [59] Simon H. Kohl, David M. A. Mehler, Michael Lührs, Robert T. Thibault, Kerstin Konrad, and Bettina Sorger. The potential of functional near-infrared spectroscopy-based neurofeedback—a systematic review and recommendations for best practice. *Frontiers in Neuroscience*, 14, July 2020.
- [60] Yury Koush, Djalel-E. Meskaldji, Swann Pichon, Gwladys Rey, Sebastian W. Rieger, David E.J. Linden, Dimitri Van De Ville, Patrik Vuilleumier, and Frank Scharnowski. Learning control over emotion networks through connectivity-based neurofeedback. *Cerebral Cortex*, page bhv311, December 2015.

- [61] Camille Lecoffre, Christine Peretti, Amélie Gabet, Olivier Grimaud, France Woimant, Maurice Giroud, Yannick Béjot, and Valerie Olié. National trends in patients hospitalized for stroke and stroke mortality in france, 2008 to 2014. *Stroke*, 48:STROKEAHA.117.017640, 09 2017.
- [62] Stéphanie Leplaideur, Emilie Leblong, Karim Jamal, Chloé Rousseau, Annelise Moulinet Raillon, Pauline Coignard, Mireille Damphousse, and Isabelle Bonan. Short-term effect of neck muscle vibration on postural disturbances in stroke patients. *Experimental Brain Research*, 234(9):2643–2651, May 2016.
- [63] Martin A. Lindquist, Ji Meng Loh, Lauren Y. Atlas, and Tor D. Wager. Modeling the hemodynamic response function in fMRI: Efficiency, bias and mis-modeling. *NeuroImage*, 45(1):S187–S198, March 2009.
- [64] Giulia Lioi, Simon Butet, Mathis Fleury, Elise Bannier, Anatole Lécuyer, Isabelle Bonan, and Christian Barillot. A Multi-Target Motor Imagery Training Using Bimodal EEG-fMRI Neurofeedback: A Pilot Study in Chronic Stroke Patients. *Frontiers in Human Neuroscience*, 14, 2020. Publisher: Frontiers.
- [65] Giulia Lioi, Claire Cury, Lorraine Perronnet, Marsel Mano, Elise Bannier, Anatole Lécuyer, and Christian Barillot. Simultaneous EEG-fMRI during a neurofeedback task, a brain imaging dataset for multimodal data integration. *Scientific Data*, 7(1), June 2020.
- [66] Nikos K Logothetis, Jon Pauls, Mark Augath, Torsten Trinath, and Axel Oeltermann. Neurophysiological investigation of the basis of the fmri signal. *Nature*, 412(6843):150–157, 2001.
- [67] Anatole Lécuyer, Fabien Lotte, Richard Reilly, Robert Leeb, Michitaka Hirose, and Mel Slater. Brain-computer interfaces, virtual reality, and videogames. *Computer*, 41:66–72, 11 2008.
- [68] C. Magri, U. Schridde, Y. Murayama, S. Panzeri, and N. K. Logothetis. The amplitude and timing of the BOLD signal reflects the relationship between local field potential power at different frequencies. *Journal of Neuroscience*, 32(4):1395–1407, January 2012.
- [69] Marco Marino, Quanying Liu, Silvia Brem, Nicole Wenderoth, and Dante Mantini. Automated detection and labeling of high-density eeg electrodes from structural mr images. *Journal of neural engineering*, 13(5):056003, 2016.
- [70] Anna-Maria Marx, Ann-Christine Ehlis, Adrian Furdea, Martin Holtmann, Tobias Banaschewski, Daniel Brandeis, Aribert Rothenberger, Holger Gevensleben, Christine M. Freitag, Yvonne Fuchsenger, Andreas J. Fallgatter, and Ute Strehl. Near-infrared spectroscopy (nirs) neurofeedback as a treatment for children with attention deficit hyperactivity disorder (adhd)—a pilot study. *Frontiers in Human Neuroscience*, 8:1038, 2015.
- [71] Camille Maumet. *From group to patient-specific analysis of brain function in arterial spin labelling and BOLD functional MRI*. Theses, Université Rennes 1, May 2013.
- [72] Camille Maumet, Pierre Maurel, Elise Bannier, Jean-Christophe Ferré, and Christian Barillot. A contrario detection of focal brain perfusion abnormalities based on an Arterial Spin Labeling template. In *9th IEEE International Symposium on Biomedical Imaging (ISBI)*, pages 1176–1179, Barcelona, Spain, May 2012.

- [73] Camille Maumet, Pierre Maurel, Jean-Christophe Ferré, and Christian Barillot. An a contrario approach for the detection of activated brain areas in fMRI. In *International Society for Magnetic Resonance in Medicine 21st Annual Meeting & Exhibition (ISMRM)*, page 3260, Salt Lake City, United States, April 2013.
- [74] Camille Maumet, Pierre Maurel, Jean-Christophe Ferré, and Christian Barillot. Robust perfusion maps in Arterial Spin Labeling by means of M-estimators. In *International Society for Magnetic Resonance in Medicine 21st Annual Meeting & Exhibition (ISMRM)*, page 3037, Salt Lake City, United States, April 2013.
- [75] Camille Maumet, Pierre Maurel, Jean-Christophe Ferré, and Christian Barillot. Robust estimation of the cerebral blood flow in arterial spin labelling. *Magnetic Resonance Imaging*, 32(5):497 – 504, June 2014.
- [76] Camille Maumet, Pierre Maurel, Jean-Christophe Ferré, and Christian Barillot. An a contrario approach for the detection of patient-specific brain perfusion abnormalities with arterial spin labelling. *NeuroImage*, 134, July 2016.
- [77] Camille Maumet, Pierre Maurel, Jean-Christophe Ferré, Béatrice Carsin, and Christian Barillot. Patient-specific detection of perfusion abnormalities combining within-subject and between-subject variances in Arterial Spin Labeling. *NeuroImage*, 81C:121–130, May 2013.
- [78] Cédric Meurée. *Arterial spin labelling: quality control and super-resolution*. Theses, Université Rennes 1, March 2019.
- [79] Cédric Meurée, Pierre Maurel, Elise Bannier, and Christian Barillot. Patch-based super-resolution for arterial spin labeling MRI. In *ISMRM 25th Annual Meeting & Exhibition*, Honolulu, United States, April 2017.
- [80] Cédric Meurée, Pierre Maurel, Jean-Christophe Ferré, and Christian Barillot. Patch-Based Super-Resolution of Arterial Spin Labeling Magnetic Resonance Images. *NeuroImage*, 189:85–94, January 2019.
- [81] Matthias Moosmann et al. Joint independent component analysis for simultaneous EEG–fMRI: principle and simulation. *Int. J. of Psychophysiology*, 67(3):212–221, 2008.
- [82] Jeanette A Mumford and Thomas Nichols. Simple group fMRI modeling and inference. *NeuroImage*, 47(4):1469–1475, 2009.
- [83] Saman Noorzadeh, Pierre Maurel, Thomas Oberlin, Rémi Gribonval, and Christian Barillot. Multi-modal EEG and fMRI Source Estimation Using Sparse Constraints. In *MICCAI 2017 - 20th International Conference on Medical Image Computing and Computer Assisted Intervention*, Quebec, Canada, September 2017.
- [84] Thomas Oberlin, Christian Barillot, Rémi Gribonval, and Pierre Maurel. Symmetrical EEG-FMRI Imaging by Sparse Regularization. In *EUSIPCO – 23rd European Signal Processing Conference*, pages pp. 1–5, Nice, France, August 2015.

- [85] R.D. Pascual-Marqui, C.M. Michel, and D. Lehmann. Low resolution electromagnetic tomography: a new method for localizing electrical activity in the brain. *International Journal of Psychophysiology*, 18(1):49 – 65, 1994.
- [86] Lorraine Perronnet, Anatole Lécuyer, Fabien Lotte, Maureen Clerc, and Christian Barillot. Brain training with neurofeedback. In *Brain-Computer Interfaces 1*. Wiley-ISTE, July 2016.
- [87] Lorraine Perronnet, Anatole Lécuyer, Marsel Mano, Elise Bannier, Fabien Lotte, Maureen Clerc, and Christian Barillot. Unimodal versus bimodal EEG-fMRI neurofeedback of a motor imagery task. *Frontiers in Human Neuroscience*, 11, April 2017.
- [88] Lorraine Perronnet, Anatole Lécuyer, Marsel Mano, Mathis Fleury, Giulia Lioi, Claire Cury, Maureen Clerc, Fabien Lotte, and Christian Barillot. Learning 2-in-1: Towards integrated eeg-fmri-neurofeedback. *bioRxiv*, 2020.
- [89] Caroline Pinte, Mathis Fleury, and Pierre Maurel. Deep learning-based localization of EEG electrodes within MRI acquisitions. working paper or preprint, May 2021.
- [90] Russell A. Poldrack, Jeanette Mumford, and Thomas Nichols. *Handbook of functional MRI data analysis*. Cambridge University Press, Cambridge, 2011.
- [91] Maïa Proisy. *Étude de la perfusion cérébrale par Arterial Spin Labeling en IRM à 1.5T chez le nouveau-né et l'enfant*. Theses, Université Rennes 1, December 2018.
- [92] Maïa Proisy, Bertrand Bruneau, C Rozel, C Tréguier, Kamal Chouklati, L Riffaud, P Darnault, and J.-C Ferré. Arterial spin labeling in clinical pediatric imaging. *Diagnostic and interventional imaging*, 97, 10 2015.
- [93] Maïa Proisy, Isabelle Corouge, Antoine Legouhy, Amélie Nicolas, Valérie Charon, Nadia Mazille, Stéphanie Leroux, Bertrand Bruneau, Christian Barillot, and Jean-Christophe Ferré. Changes in brain perfusion in successive arterial spin labeling mri scans in neonates with hypoxic-ischemic encephalopathy. *NeuroImage: Clinical*, 24:101939, 07 2019.
- [94] Olaf Ronneberger, Philipp Fischer, and Thomas Brox. U-net: Convolutional networks for biomedical image segmentation. In *International Conference on Medical image computing and computer-assisted intervention*, pages 234–241. Springer, 2015.
- [95] MJ Rosa et al. EEG-fMRI integration: a critical review of biophysical modeling and data analysis approaches. *J. of integrative neuroscience*, 9(04):453–476, 2010.
- [96] François Rousseau. A non-local approach for image super-resolution using intermodality priors. *Medical Image Analysis*, 14(4):594–605, 2010.
- [97] René Scheeringa, Pascal Fries, Karl-Magnus Petersson, Robert Oostenveld, Iris Grothe, David G. Norris, Peter Hagoort, and Marcel C.M. Bastiaansen. Neuronal dynamics underlying high- and low-frequency eeg oscillations contribute independently to the human bold signal. *Neuron*, 69(3):572–583, 2011.

- [98] Benoit Scherrer, Ali Gholipour, and Simon Warfield. Super-resolution reconstruction to increase the spatial resolution of diffusion weighted images from orthogonal anisotropic acquisitions. *Medical image analysis*, 16:1465–76, 06 2012.
- [99] Marta Segarra, Bettina C. Kirchmaier, and Amparo Acker-Palmer. A vascular perspective on neuronal migration. *Mechanisms of Development*, 138:17 – 25, 2015. Neurovascular unit.
- [100] R.E. Shiffler. Maximum Z scores and outliers. *The American Statistician*, 1988.
- [101] David Shuman, Sunil K. Narang, Pascal Frossard, Antonio Ortega, and Pierre Vandergheynst. The emerging field of signal processing on graphs: Extending high-dimensional data analysis to networks and other irregular domains. *IEEE Signal Processing Magazine*, 30, 10 2012.
- [102] Karam Sidaros, Kern Olofsson, Maria J Miranda, and Olaf B Paulson. Arterial spin labeling in the presence of severe motion. *J Cereb Blood Flow Metab*, 2005.
- [103] Tuomas Tallinen, Jun Chung, François Rousseau, Nadine Girard, Julien Lefèvre, and Lakshminarayanan Mahadevan. On the growth and form of cortical convolutions. *Nature Physics*, 12, 02 2016.
- [104] Huan Tan, Joseph A Maldjian, Jeffrey M Pollock, Jonathan H Burdette, Lucie Y Yang, Andrew R Deibler, and Robert A Kraft. A fast, effective filtering method for improving pulsed arterial spin labeling MRI. *Journal of Magnetic Resonance Imaging*, 29(5):1134–9, 2009.
- [105] Corentin Vallée. *Arterial spin labeling performance in resting-state functional MRI: the effect of scan duration*. Theses, Université de rennes 1, June 2020.
- [106] Corentin Vallée, Pierre Maurel, Isabelle Corouge, and Christian Barillot. Resting-state ASL: Toward an optimal sequence duration. In *ISMRM 2018 - International Society for Magnetic Resonance in Medicine*, pages 1–2, Paris, France, June 2018.
- [107] Corentin Vallée, Pierre Maurel, Isabelle Corouge, and Christian Barillot. Acquisition duration in resting-state arterial spin labeling. How long is enough? *Frontiers in Neuroscience*, July 2020.
- [108] Gael Varoquaux, Alexandre Gramfort, Fabian Pedregosa, Vincent Michel, and Bertrand Thirion. Multi-subject dictionary learning to segment an atlas of brain spontaneous activity. volume 22, pages 562–73, 07 2011.
- [109] Curtis R Vogel. *Computational methods for inverse problems*, volume 23. Siam, 2002.
- [110] Jiongjiong Wang, Daniel J. Licht, Geon-Ho Jahng, Chia-Shang Liu, Joan T. Rubin, John Haselgrove, Robert A. Zimmerman, and John A. Detre. Pediatric perfusion imaging using pulsed arterial spin labeling. *Journal of Magnetic Resonance Imaging*, 18(4):404–413, 2003.
- [111] Tianlu Wang, Dante Mantini, and Celine Gillebert. The potential of real-time fmri neurofeedback for stroke rehabilitation: A systematic review. *Cortex*, 107, 09 2017.

- [112] Christopher Whalen, Edward L Maclin, Monica Fabiani, and Gabriele Gratton. Validation of a method for coregistering scalp recording locations with 3d structural mr images. *Human brain mapping*, 29(11):1288–1301, 2008.
- [113] Max Wintermark, Musa Sesay, Emmanuel Barbier, Katalin Borbély, Wiilliam Dillon, James Eastwood, Thomas Glenn, Cécile Grandin, Salvador Pedraza, Jean-François Soustiel, Tadashi Nariai, Greg Zaharchuk, Jean-Marie Caillé, Vincent DOUSSET, and Howard Yonas. Comparative overview of brain perfusion imaging techniques. *Stroke; a journal of cerebral circulation*, 36:e83–99, 10 2005.
- [114] Joseph Woods, Michael Chappell, and Thomas Okell. Designing and comparing optimized pseudo-continuous arterial spin labeling protocols for measurement of cerebral blood flow. *NeuroImage*, 223:117246, 08 2020.
- [115] Joseph G. Woods, Michael A. Chappell, and Thomas W. Okell. A general framework for optimizing arterial spin labeling mri experiments. *Magnetic Resonance in Medicine*, 81(4):2474–2488, 2019.
- [116] Lei Yu, Pierre Maurel, Christian Barillot, and Rémi Gribonval. Compressive Matched Filter for Cerebral Blood Flow Quantification with ASL: sampling diversity or repetition? In *Miccai Workshop on Sparsity Techniques in Medical Imaging (STMI'12)*, pages 0–0, Nice, France, October 2012.
- [117] Jennifer Zechel, Michael Buczek, Jorge Gamboa, Michelle Puchowitz, and Wesley Lust. Impact of chronic prenatal intermittent hypoxia on neuronal migration. *Journal of Cerebral Blood Flow & Metabolism*, 25, 08 2005.
- [118] Catharina Zich, Stefan Debener, Cornelia Kranczioch, Martin G. Bleichner, Ingmar Gutberlet, and Maarten De Vos. Real-time EEG feedback during simultaneous EEG–fMRI identifies the cortical signature of motor imagery. *NeuroImage*, 114:438–447, July 2015.
- [119] Catharina Zich, Stefan Debener, Ann-Kathrin Thoene, Ling-Chia Chen, and Cornelia Kranczioch. Simultaneous EEG–fNIRS reveals how age and feedback affect motor imagery signatures. *Neurobiology of Aging*, 49:183–197, January 2017.
- [120] Vadim Zotev, Raquel Phillips, Han Yuan, Masaya Misaki, and Jerzy Bodurka. Self-regulation of human brain activity using simultaneous real-time fmri and eeg neurofeedback. *NeuroImage*, 85, 05 2013.